ABSTRACT

Title of Thesis: IMAGING PYROMETRY OF SMOLDERING
                                    WOOD EMBERS AT VARIOUS DISTANCES
                                    AND ILLUMINATIONS

                                    Kyle Decker, Master of Science, 2021

Thesis Directed By: Dr. Peter B. Sunderland
                                    Department of Fire Protection Engineering

Wildland fires in the WUI present a constant threat to life and property in the United States and across the globe. Many wildland fires are caused by ember spotting, a process in which firebrands are lofted significant distances away from the fire front by combinations of winds and gas flows. These firebrands have the potential to collect and cause new spot fires independent of the original wildland fire. While firebrand mechanisms such as ember generation and transport have been thoroughly studied and quantified, the capacity in which firebrands cause these fires is not as well known. Recent studies have made progress towards determining the surface temperature of these firebrands; however, none have provided repeatable temperature data from a variety of test conditions. This paper presents firebrand surface temperature using color imaging ember pyrometry techniques for various imaging distances and illuminations. A digital color camera was calibrated to a blackbody furnace with a temperature range of 600 – 1200 °C. Calibration to the blackbody allows the normalized pixel values of each image to be converted to temperature using G/R ratio, grayscale, and hybrid pyrometry. Signal to noise ratios of around 850 and 46 for grayscale and ratio pyrometry were obtained. Two simultaneous images of a single ember from distances of 0.5 and 1 m, as well as additional images from 4 m were observed and quantified. The firebrand surface temperature was determined to be independent of imaging distance. The mean

surface temperature across all imaging distances was calculated to be 931 ± 6.2 °C. Ratio pyrometry was observed to be the preferred method of imaging pyrometry due to its independence from surface emissivity and transmissivity as well as it's applicability to real fire scenarios for future research. Firebrands were also imaged in sequences containing various illumination and background color. Illumination was observed to disrupt G/R ratio pyrometry due to an overwhelming increase in green pixel values.

IMAGING PYROMETRY OF SMOLDERING WOOD FIREBRANDS AT VARIOUS
DISTANCES AND ILLUMINATIONS

by

Kyle Decker

Thesis submitted to the Faculty of the Graduate School of the
University of Maryland, College Park, in partial fulfillment
of the requirements for the degree of
Master of Science
2020

Advisory Committee:
Dr. Peter B. Sunderland, Chair/Advisor
Dr. Stanislav I. Stoliarov
Dr. Arnaud Trouvé

Acknowledgements

There are many people who I must thank for helping me throughout my time completing this research project. First, I must thank my advisor Dr. Peter B. Sunderland who has made my participation on this research project possible. I would like to thank him for going out of his way to bring me in to his research group on short notice and making the transition from an undergraduate student to a graduate student as seamless as it could be. I could not ask for a more thoughtful and positive advisor, who's door is always open for questions and concerns no matter the situation. To all of the people over at NIST, thank you for providing me with the opportunity to complete this research.

I would like to thank all of the fire protection engineering faculty for supporting me ever since the day I entered the department as an undergraduate. To Nicole Hollywood, without you our department would not be the same. Thank you for always being there for help inside and outside of school whenever I needed it, I'll always be grateful for everything you've done for me along the way. To all of my professors who have spent their valuable time educating me on new challenging topics every day, my teenage self would have never believed that school could actually be fun one day which all of you played a part in making happen. To Fernando, thank you for always being there and helping me out in the lab no matter how basic the questions I had.

After nearly four years in the fire protection engineering department, the most rewarding part along the way was all of the relationships and bonds created with my fellow students. To Garrett Wack and Jenn Wood, who were the two people I knew in fire protection before I transferred in, who were always there for me inside and outside of the classroom. In my early days as an undergraduate through my first semester in fire protection, Garrett always took the time and effort to come sit with me in our lectures when I was usually just hanging out in the back by myself.

I'll never be able to repay the kindness you showed me along the way. To Ella, Chris, Yannick, Angad, Josh, and Patrick just to name a few, I'll never forget the journey through our undergraduate days. To Joey, Will, Ashlynne, and Michael, I'm honored to have transitioned to grad school with you all and I definitely would not have gotten through without your help. To the many students I met in Dr. Sunderland's group and throughout the department in graduate school, I was constantly motivated by all of your brilliance and kindness along the way. To all of the students I had the pleasure of tutoring and serving as a TA for, you all made the time put in very well spent.

Lastly, to my family and friends from home, thank you for always supporting me in whatever I choose to take on in life. To my Mom and Dad, for always being there by my side, to the short notice rides home to Catonsville, to the steadfast love and support, I always be thankful. To my sister, for always being there with the cats when I need it even when I pester you with annoyance. While I may be much taller, you will always be my big twin sister. To Pop Pop, thank you for always going out of your way for me in ways big and small, whether it's always making sure I've got something to eat or swinging by with another classic bobblehead. To the crew back home, I could never put into words all of the amazing time spent with you all. All of the laughs and adventures make life worth living.

Table of Contents

List of Figures

Chapter 1: Introduction

1.1. Literature Review

Wildland fires present an increasing destructive issue to communities across the globe. As our global population and society grows in size, the threats posed by wildfires against the Wildland-Urban Interface (WUI) continue to mount [1,2]. Recent years have seen some of the most destructive wildfires in history, especially in the California area [3,4]. In 2018, California saw its deadliest and most destructive fire in history as the Camp Fire raged through California, destroying 18,804 structures and killing 85 civilians [3].

One area impacting wildfires that is of particular interest is fires caused by firebrands. Firebrands are classified as any burning piece of material, typically wood, that travel through the air. The challenge presented by firebrands is that they can travel long distances ahead of a wildfire and ignite spot fires [5-8]. Reference [5] identifies multiple fires affecting the WUI in which firebrand shower travel played a significant role in the overall spread of the fire. Reference [7] explores the spotting ignition behavior of metal particles on wooden fuel beds, which does not match the typical wood material of a firebrand ember but still demonstrates the spotting ignition process seen in many WUI fires.

Significant research has been conducted on the general behavior of firebrands. The generation and transport of firebrand embers has been studied and characterized on many occasions [9-11]. Reference [10] develops a predictive model for the trajectory of multiple shape configurations of firebrands based off conditions typically seen in a wildland fire. The mechanisms in which firebrands ignite common materials has been widely observed [12-17]. References [12,13] investigate the ignition of typical roof and deck assemblies of the WUI via firebrand

showers. Reference [14] discusses how the heat transfer between firebrands and typical fuel sources is affected by the contact points between the two.

The usage of color pyrometry to determine surface temperature has been used extensively across various applications. The output signal of a detector is related to the temperature of the target surface according to a transfer function, normally obtained by calibration with a black body [25]. Detector calibration is often completed using a target blackbody surface or direct calculation of Planck's Law [18-19,27-28,33-38], but has also been completed using thermocouple measurements [35]. Usage of a single signal requires complete knowledge of the components causing signal attenuation between the target surface and the detector. A common example of a single signal detector would be an IR camera, which is commonly used to determine temperature [8,20,21]. This is often avoided through the usage of color ratio pyrometry, which uses a ratio of two different signals on a detector to eliminate the dependence on emissivity and transmissivity of the grey surface. The most common signal used in color pyrometry involves the blackbody emissive power, commonly referred to as Planck's Law, integrated over a spectral wavelength range and corrected for the non-blackbody behavior of the surface in question and sensor sensitivity [19,33-34,36-37]. Reference [33] uses multicolor band pyrometry to determine char particle surface temperature with digital color cameras of CMOS and CCD sensor types. Reference [34] uses two color ratio pyrometry to determine the surface temperature of metal spark sprays. Reference [36] uses two color ratio pyrometry to determine the surface temperature of objects placed in a hypersonic flow regime. Reference [36] not only determines surface temperature with color ratio pyrometry, but also soot volume fractions in flames. Other examples of signals used in ratio pyrometry include Ref. [18], which uses a normalized pixel intensity ratio to find temperature,

as well as Ref. [38], which combines traditional RGB color pyrometry with a spectral emissivity model of char particles to determine dispersed char surface temperature.

1.2. Gaps in Literature

While attempts have been made to determine the surface temperature of firebrand or ember surface temperatures, many gaps are still present in the literature that must be addressed. Most color pyrometry methods found in the literature determine surface temperature of char or metal particles [-], with limited information present related to firebrand temperature. Measurements conducted with thermocouples have problems stemming from poor contact, surface cooling, and small measurement areas [19]. References [8,21] use an IR camera to determine temperature, and find results from 800 – 950 °C using assumed emissivity values. The primary issues with using an IR camera lie in the need to assume an emissivity value, limited pixel counts and bit depths, as well as high cost. Reference [19] obtained temperatures between 750 – 950 °C using ratio pyrometry and found significant advantages of color pyrometry over infrared imaging techniques. The methods used by Ref. [19] are similar to the methods used here, however they only measure temperature from one distance with one camera. Reference [18] obtained a mean ember temperature of around 930 °C using a hybrid of ratio and grayscale pyrometry. The hybrid pyrometry measurements made by Ref. [18] have better signal to noise ratios than Ref. [19], however measurements are only made from an even closer distance, in exclusively dark conditions from one camera.

1.3. Motivations and Objectives

Any model of flame spread or prediction of ignition behavior with firebrand spot fires relies on the surface temperature of the firebrand. Calculations of heat flux, burning rate, or flame spread velocity cannot be made without a surface temperature input. Without an accurate surface

temperature estimate, the reliability of the resulting model is significantly compromised. Traditional modeling programs like FDS require some knowledge of surface temperature to simulate burning behavior. Many wildland fire modeling programs limit themselves to flame spread caused by the direct movements of the wildland fire, completely missing out on the effects of ember spotting. An underestimate of ember surface temperature leads to a poor assessment of the hazards posed by the ember or collection of embers. The ability to accurately determine the surface temperature of an ember would go great lengths in improving fire protection methods put forth to protect society from wildland fires.

The primary objective of this thesis is to determine the surface temperature of a single ember from multiple imaging distances. Identifying a pyrometer whose surface temperature results are independent of distance would be a significant advancement for performing firebrand pyrometry. Confirming the temperatures observed by Refs. [18,19] over multiple larger distances would enhance the reliability of those surface temperature results. Another objective of this thesis is to determine the surface temperature of a firebrand at multiple distances with added illumination to the testing environment. While completing this objective is not entirely necessary for the reliability of surface temperature measurements, it would allow further research to be conducted with the same pyrometry methods used in these experiments on firebrand embers outside the laboratory setting. In a real wildland fire, firebrands cannot be imaged in full darkness from less than a 1 m distance. Proving that an inexpensive color camera pyrometer is consistent across distance and illumination would significantly enhance the applicability to further firebrand research and field use.

Chapter 2: Camera Calibration

2.1. Introduction

This chapter demonstrates how the color cameras are calibrated with a blackbody furnace. The camera model is the Sony DSC-RX10 III. Camera 1 was previously calibrated by Ref. [18]. Camera 1 was re-calibrated here, while Camera 2 was calibrated for the first time. Red, green, and blue pixel values were evaluated at various temperatures, exposure times, and distances. Pixel values were normalized to account for differences in camera settings. Curve fits using the logarithmic green to red normalized pixel ratio were developed for ratio pyrometry. Curve fits using the logarithm of the normalized grayscale value were developed for grayscale pyrometry.

2.2. Experimental

The primary components for camera calibration include the digital camera used for imaging, and a blackbody furnace. Additional components used include metal posts and brackets for camera mounting. A tape measure was used to determine the distance from camera lens to the inner face of the blackbody emitter.

Fig. 2.1. Experimental setup of the camera calibration to the blackbody emitter.

Both cameras used were the Sony DSC-RX10 III compact digital camera. This model includes a 13.2×8.9 mm Exmor RS® CMOS sensor, a pixel count of approximately 20.1 megapixels, and a bit depth of 14 in each plane [22]. The lens is a Zeiss® Vario-Sonnar® T* 24–600 mm, f2.4–4 large-aperture zoom lens [22]. No filters were used, and all images were taken in a RAW format. All blackbody images were taken with no additional zoom magnification, with the camera focus centered on the middle

of the blackbody furnace aperture. No additional zoom keeps the camera f-number at a constant 2.4. While the camera ISO limit stretches from 64 to 12800, the ISO for all blackbody images was held at 100.

The blackbody furnace was an Oriel 67032 model blackbody infrared light source. The aperture cavity opening is 25.4 mm, with an operating temperature range of 50-1200 ±0.2 °C. The emissivity of the blackbody furnace surface is 0.99 ± 0.01, which is confirmed in a study from Ref. [27].

2.3. Procedures

Reference [18] developed calibration curves for one of the camera's used, at a distance of 4.2 cm from the blackbody furnace. This camera, referred to as Camera 1, was re-calibrated here at the same distance as its original calibration. Camera 2, which is a newer version of Camera 1, was used for the first time here. Camera 2 was calibrated for a temperature range of 600-1100 °C and distances of 0.042, 1, and 2 m. Exposure time was altered to allow pixel values to be as high as possible without approaching a saturated pixel value of 65535.

The RAW images taken of the blackbody were recorded, then converted from RAW files to 16-bit TIFF files using dcraw software [24]. Inputs used for dcraw were "-4", "-T", and "-v". The "-4" command writes the file to the 16-bit linear format, the "-T" writes the file to a tiff format, and the "-v" command prints out messages in the command script. The TIFF files were opened in NIH's image analysis program ImageJ. For each image, a square in the middle of the blackbody aperture was analyzed, where the pixel values of the blackbody are most accurate due to vignetting. For the 0.042, 1, and 2 m camera distances, this range was chosen to be 200×200, 20×20, and 10×10 pixels, respectively. The mean pixel value in the red, green, and blue channels for this square region was taken for each image, and assigned to the I_R, I_G, and I_B for that respective image.

2.4. Results

Images of the blackbody were taken with both Camera 1 and Camera 2 to calibrate image pixel value to temperature. Figure 2.2 shows the red, green, and blue pixel values at a distance of 4.2 cm away from the blackbody and a temperature of 800 °C. Only the red channel of the RGB space approached pixel saturation, with any blackbody results reaching saturation in the red channel being discarded. The re-calibration of Camera 1 matches the original calibration from Ref. [18] almost exactly, with pixel values in the red, green, and blue channels typically varying by at or less than 5%. Blue pixel values at the faster exposure times tend to exhibit more noise due to the very small pixel value magnitudes. Red pixel values are observed to be larger for Camera 2 than Camera 1 at the same imaging conditions. Due to observed differences in red, green, and blue pixel values, unique calibration curves for Camera 2 were developed.

Figure 2.3 shows the red, green, and blue pixel values at a temperature of 800 °C and distances of 4.2 cm, 1 m, and 2 m away from the blackbody. All images displayed in Fig. 2.3 are from Camera 2. In each color channel, pixel values increase linearly as exposure time grows, with little dependence on the camera's distance away from the blackbody. Small variations in pixel values are seen in the green and blue channels at higher exposure times. These variations may be neglected as increases in one color are accounted for in a similar decrease in another. The number of usable pixels for the calculation of mean pixel value in each color channel is much higher for the 4.2 cm distance, leading to lower standard deviations at each exposure time. Even with lower standard deviations, the mean pixel value at each exposure time in each color channel is very similar for each tested distance.

7
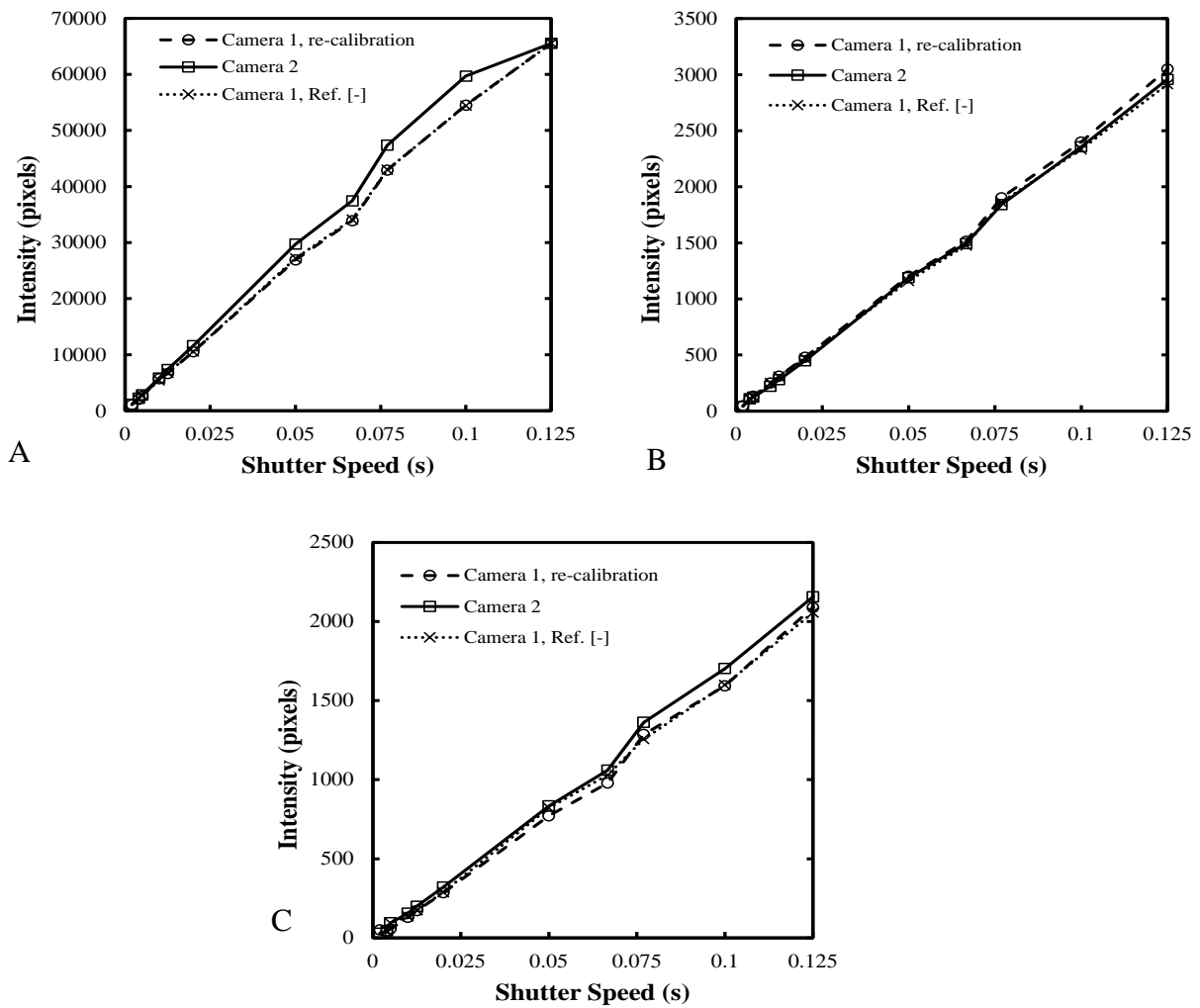
Fig. 2.2. Pixel values plotted with respect to exposure time for Camera 1 and Camera 2 at a blackbody temperature of 800 °C and 4.2 cm from the blackbody aperture. (a) Red color channel (b) Green color channel (c) Blue color channel
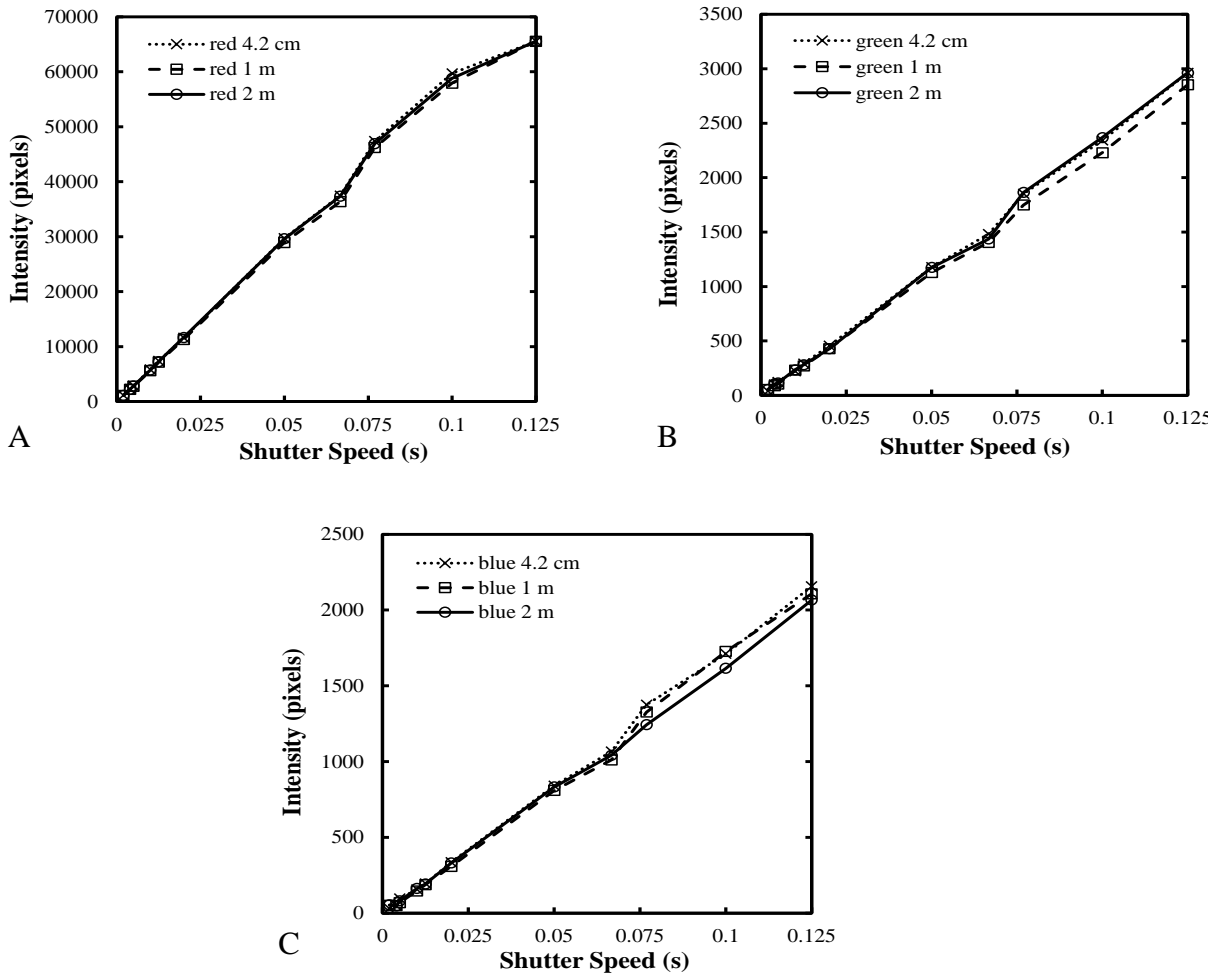
Fig. 2.3. Pixel values plotted with respect to exposure time for Camera 2 at a blackbody temperature of 800 °C and 4.2 cm, 1 m, and 2 m from the blackbody aperture. (a) Red color channel (b) Green color channel (c) Blue Color Channel

Figure 2.4 shows the normalized pixel value in the red, green, blue, and grayscale color planes for Camera 1 and Camera 2, as well as the spectral emissive power of an ideal blackbody at wavelengths of 430 and 680 nm. The grayscale pixel value, I_{GS}, is found by the equation:

$$I_{GS} = (I_R + I_G + I_B) / 3 , \tag{1}$$

where I_R, I_G, and I_B are the red, green, and blue pixel values, respectively. The normalized pixel value, NI_i, is found using the equation recommended by Ref. [18]:

$$NI_i = (I_i - I_{i,DC}) f^2 / t \, ISO , \tag{2}$$

where $I_{i,DC}$ is the dark current pixel value in the relevant color plane, f is the camera f-number

9

(commonly referred to as f-stop), t is the camera exposure time, and *ISO* is the camera ISO brightness setting. The subscript , i, represents the color channel of interest. At a given temperature, multiple combinations of camera settings may yield the same raw pixel value in either the red, green, or blue color channel. The normalized pixel value is used instead of raw pixel value to account for differences in camera settings. By normalizing the pixel value, images taken with any range of the relevant camera properties can be compared. The normalized value of the red color plane is 2-3 orders of magnitude higher than the green and blue color planes, which is to be expected from naked eye observation of the glowing red blackbody aperture. At the low end of the tested temperature range, the normalized blue value is an order of magnitude larger than the normalized green value. From the middle to upper end of the temperature spectrum, that pattern flips to green being larger than the blue. The normalized grayscale value curve almost identically matches the shape of the red curve, which is expected due to red pixel values consistently being much larger than the green and blue channels as observed in Fig. 2.2. The spectral emissive power of an ideal blackbody is found using the equation suggested by Ref. [18]:

$$E_\lambda = C_1 / (\lambda^5)exp(C_2 / \lambda T) , \qquad (3)$$

where C_1 and C_2 are the first and second radiation constants, which are 3.742×10^{-16} Wm^2 and 0.01439 mK respectively, λ is wavelength, and T is temperature. The spectral emissive power at wavelengths of 430 and 680 nm are plotted in Fig. 2.4, representing the responding wavelength range of Camera 1 and Camera 2. The normalized pixel value curves in Fig. 2.4 match the shape of both E_{430nm} and E_{680nm}, while also remaining within the magnitude range between the E_{430nm} and E_{680nm} curves. By matching shape and range, the normalized pixel values of the red, green, and blue color planes may be used for color pyrometry [18,19,25].

Figure 2.5 plots temperature with respect to three normalized color ratios. The three ratios plotted are each considered for ratio pyrometry. The B/R ratio curve is far too flat to yield a reasonable signal to noise ratio. Reference [25] suggests that for surface pyrometry, radiation measurements should be made at two difference monochromatic wavelengths. Due to its monotonic increase with temperature, the G/R curve is the only one exhibiting no overlapping wavelengths. Refs. [18] and [28] both suggest the G/R curve fit for ratio pyrometry for the tested temperature range.
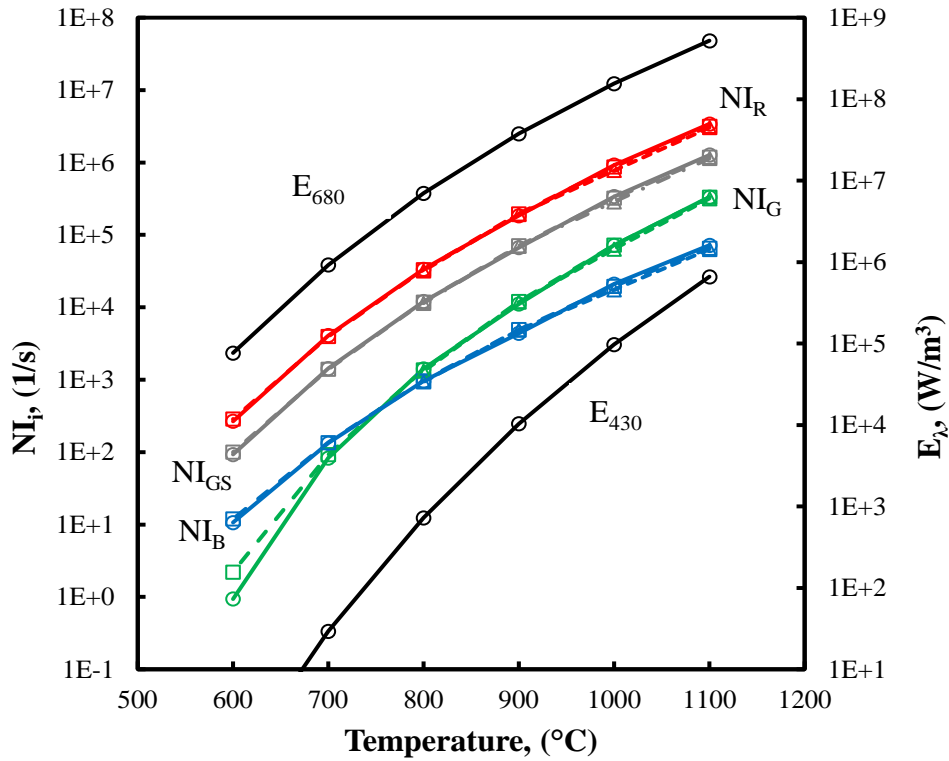
Fig. 2.4. Normalized pixel values and blackbody spectral emissive power plotted with respect to temperature.
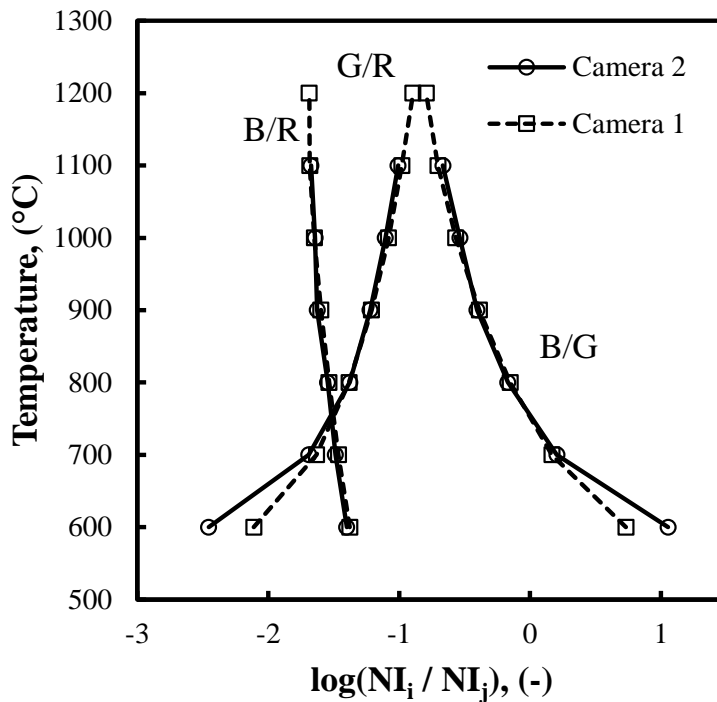
Fig. 2.5. Temperature plotted with respect to the logarithmic ratio of normalized pixel values.

Figures 2.6 and 2.7 show the curve fits for ratio and grayscale pyrometry, respectively, for both Camera 1 and Camera 2. The pixels used for these curves were the exposure times that bring the red values just under saturation. Both curve fits in Fig. 2.6 are 3rd order best fit polynomials, with good agreement between both cameras from 700 °C to the upper limit of the temperature range. Variations in curve fits grow below 700 °C due to normalized green pixel values at 600 °C for the new camera appearing lower than expected. As seen in Fig. 2.4, the slope of the normalized green pixel value curve increases as temperature decreases. With raw green pixel values appearing around 300 as the red channel approaches saturation, increased noise for the G/R fit at the low end of the temperature range are expected. The G/R ratio values at each temperature were calculated using the images for that temperature yielding the red pixel values closest but still below the saturation value. Both curve fits in Fig. 2.7 are 2nd order best fit polynomials, with good agreement

12

between both cameras over the entire temperature range. Curve fits for Camera 2 were applied to the 10 x 10 pixel regions analyzed at each blackbody temperature, yielding signal to noise ratios of around 850 and 46 for grayscale and ratio pyrometry, respectively.
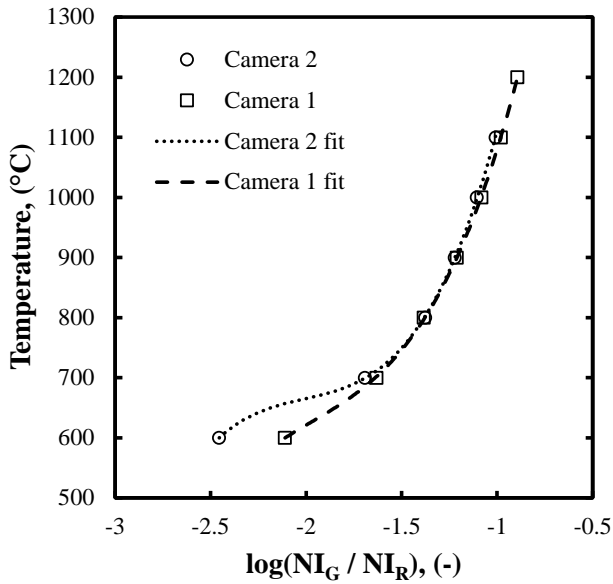
Camera 1:

$y = 292.26x^3 + 1733.8x^2 + 3614.5x + 3253.2$

$R^2 = 0.9999$

Camera 2:

$y = 362.73x^3 + 2186.7x^2 + 4466.5x + 3753.5$

$R^2 = 0.9999$

Fig. 2.6. Temperature plotted with respect to the logarithmic ratio of the normalized green pixel value to the normalized red pixel value.
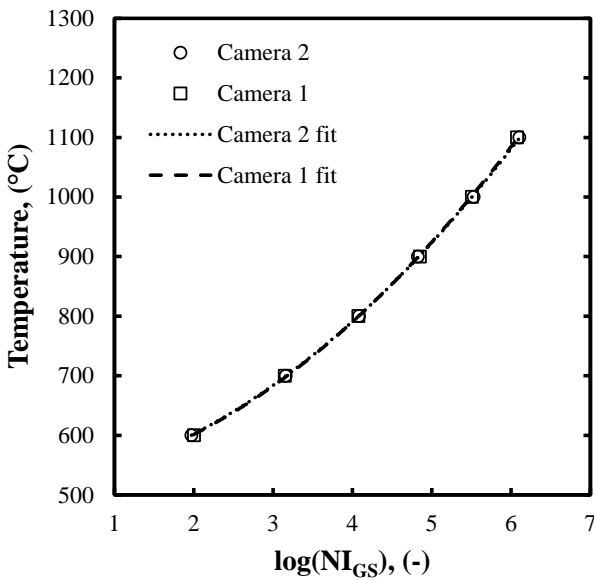
Camera 1:

$y = 13.126x^2 + 15.692x + 517.63$

$R^2 = 0.9998$

Camera 2:

$y = 12.622x^2 + 18.54x + 514.93$

$R^2 = 0.9999$

Fig. 2.7. Temperature plotted with respect to the logarithm of the normalized grayscale pixel value.

Chapter 3: Ember Temperatures Across Various Imaging Distances

3.1. Introduction

This chapter identifies the surface temperature of two primary embers using ratio, grayscale, and hybrid pyrometry. Two primary phases of experiments are included in this chapter. The first phase consists of the simultaneous imaging of two burning embers from distances of 0.5 and 1 m. The second phase consists of imaging of two more embers from a 4 m distance. The relationship between each method of pyrometry as well as the effect distance has on surface temperature calculation through pyrometry is explored and quantified.

3.2. Experimental

The embers are modeled by burning wooden dowels. These are 6.35 mm diameter maple rods manufactured by McMaster-Carr. These rods were cut into 20 mm samples using a vertical band saw. Sandpaper was used to gently smoothen any rough cuts on the sides of each piece. A lathe was used to drill 3.18 mm through the axial dowel axis. The samples were mounted horizontally at a height of 26-30 cm above the table surface. Individual 10 µm diameter Sylramic SiC fibers mounted the sample

Fig. 3.1. Sample drilling via lathe machinery.

between the magnetic metal posts. Two fibers were used for each sample to form an X-shaped pattern, with each strand forming the upper and lower V-shaped structures as shown in Fig. 3.2.

Samples were dried in an oven at 100 °C for at least 24 hours prior to ignition. The ignition source was a butane lighter with a flexible head.
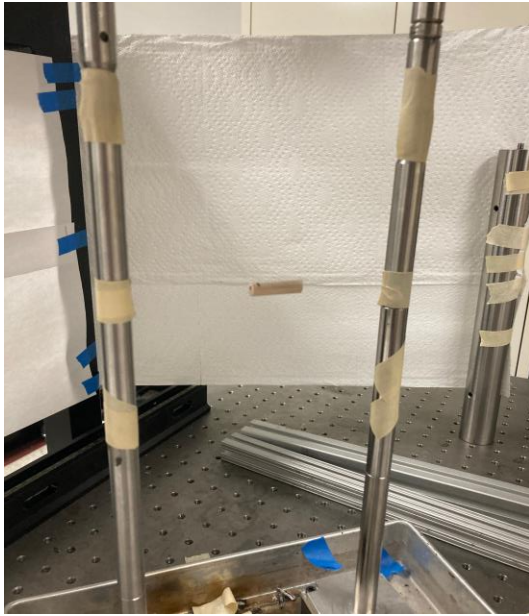

Fig. 3.2. Standard configuration of the mounted sample before ignition.
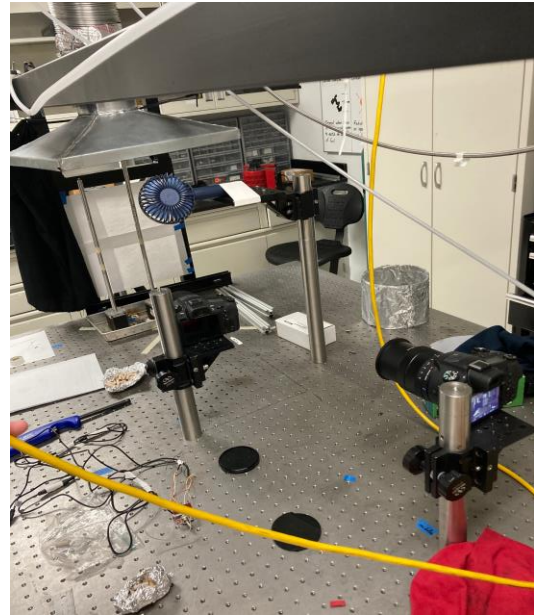
Fig. 3.3. Experimental setup for 0.5 and 1 m simultaneous imaging.
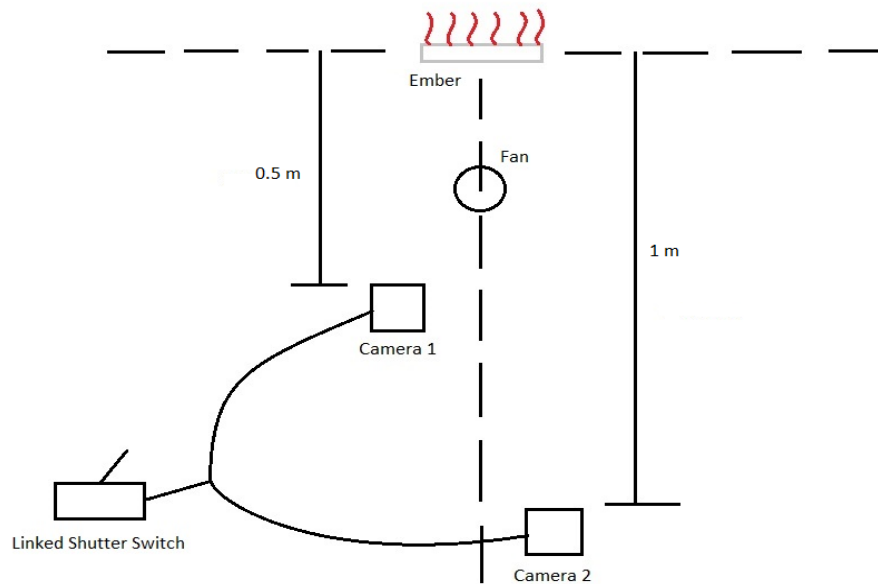
Fig. 3.4. Diagram of the experimental setup for 0.5 and 1 m simultaneous imaging.
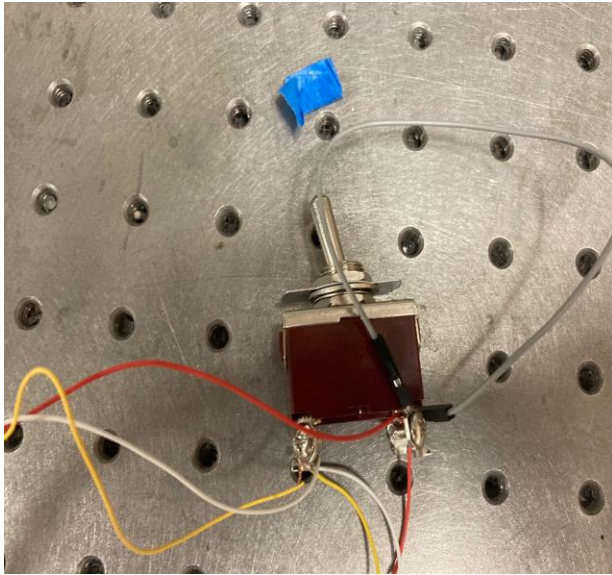
Fig. 3.5. Switch system used to trigger both cameras simultaneously.
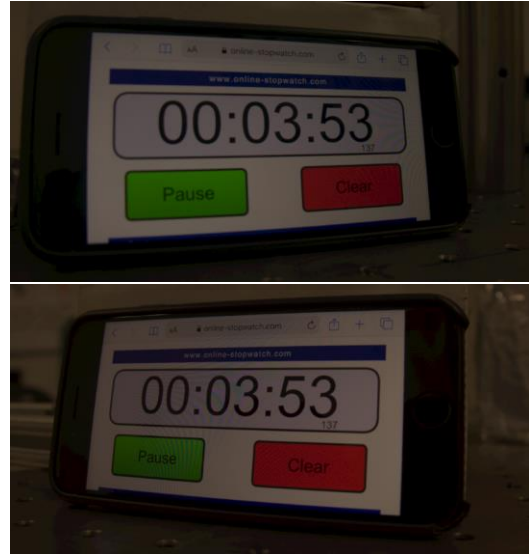
Fig. 3.6 Imaging of a stopwatch with Cameras 1 and 2 using an exposure time of 0.01 s.

Figure 3.3 shows the ember and mounting configuration of Cameras 1 and 2 for 0.5 and 1 m imaging. Screw-in metal posts and brackets were used to securely mount the cameras at distances of 0.5 and 1 m. Camera 1 was placed at the front, and Camera 2 was placed in the back. These distances were measured from the front of the ember surface to the camera lens. The cameras' optical axes were horizontal and as close as possible to perpendicular to the ember axes. A handheld fan was mounted above and in front of the embers and oriented at a 25° angle with respect to the vertical. Using a handheld rotating vane anemometer, the fan was determined to produce about 2 m/s of wind speed measured at the ember surface. Sheets of white paper were mounted behind the ember and were large enough to encompass the entire background of the burning ember and its surrounding local area.

Figure 3.5 shows the system used to trigger both cameras at the same time, accurate to 10 ms. Figure 3.6 shows simultaneous images taken with Camera 1 and Camera 2 of a stopwatch. The system consists of two remote shutter cables linked to a double pole single throw switch. The

remote shutter release cable chosen was a Kiwifotos remote control shutter release cord, compatible with a wide range of Sony cameras including the DSC-RX10 III. The toggle switch chosen was a Baomain double pole single throw switch. This switch is rated at 250 VAC/15 A and 125 VAC/20 A, with four screw terminals and a 12 mm mounting hole.

Figure 3.7 shows the setup for the second part of this chapter. An adjustable tripod was used to mount Camera 2 level with the mounted sample. Camera 2 was mounted 4 m away from the sample, directly perpendicular to the normal direction of the ember surface. This distance was measured from the front of the ember surface to the camera lens. The position of the handheld fan was identical to that explained above. Sheets of white paper were once again mounted behind the ember, parallel to the camera lens.

Fig. 3.7. Experimental setup for 4 m imaging.

Fig. 3.8. A standard image of the flaming phase of the ember burning process.

3.3. Procedures

Before ignition, the focus of both cameras was set on the face of the sample. The focus is set with the camera zoomed all the way out and the laboratory lights on. Ignition is achieved by moving the flame tip of the butane light across the base of the sample until uniform burning is observed. After ignition, the laboratory lights are turned off for the duration of the experiment. After the ember transfers from flaming combustion to smoldering, the fan was activated to aid uniform smoldering. Uniform smoldering allows the ember to glow evenly across the front face of the sample. Imaging is performed 5-10 s after fan activation. Images were taken in the RAW format and converted to 16-bit TIFF files using the same process laid out in Section 2.3. The red, green, and blue value values of each pixel were determined using MATLAB. Excel and MATLAB were both used to analyze the relevant measurements.

3.4. Results

Figure 3.9 shows Ember 1 and Ember 2 at imaging distances of 0.5 and 1 m away from the sample. All images in Fig. 14 are cropped to a range of 70×180 pixels. The original size of each image in Fig. 3.9 was 3672×5496 pixels. All images used for pyrometry in this chapter had the same camera properties. The *ISO* was set to 100, the exposure time, *t*, was set to 4 ms, and the *f*-number, *f*, was set to 2.4. Without any external illumination applied, the only visible areas in the image are the glowing parts of the ember. Small traces of black ash were observed to collect on the face of the ember. Both embers were observed to deform in some capacity. Ember 2 exhibited more deformation on the upper and lower surfaces in the x-direction, while both embers showed minor deformation in the y-direction. The visibly brightest areas of both embers are located at the far left and right ends of the sample. Ember 1 is visibly brighter in the upper areas of the ember, while the brightness of Ember 2 is more evenly distributed across the entire ember surface.

A)
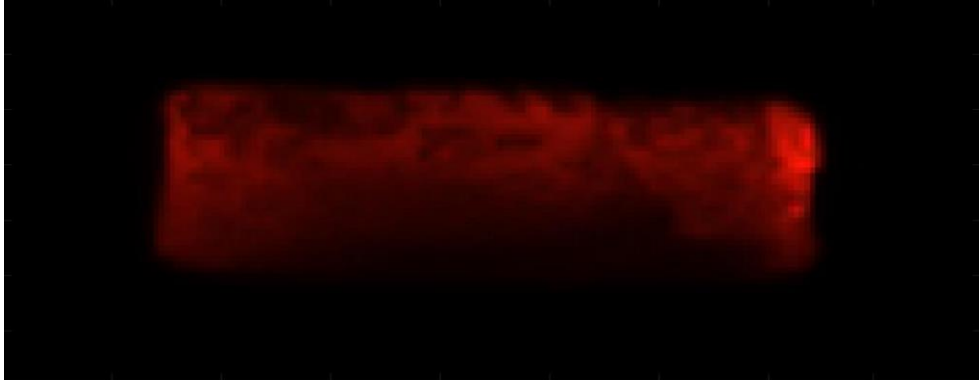
B)
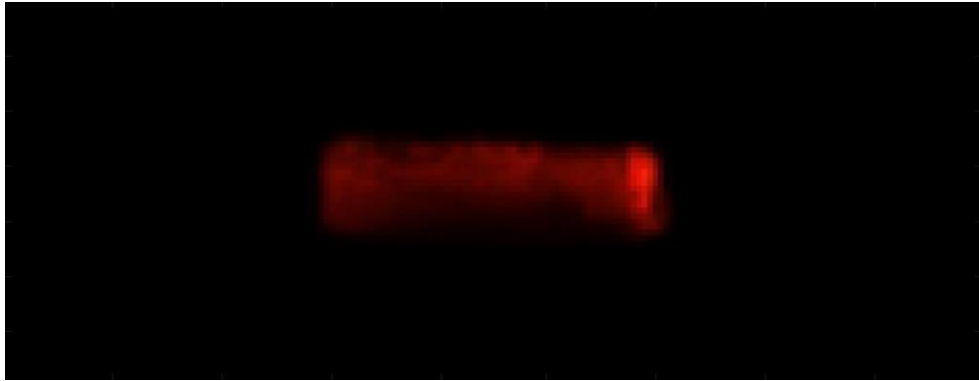
C)

D)
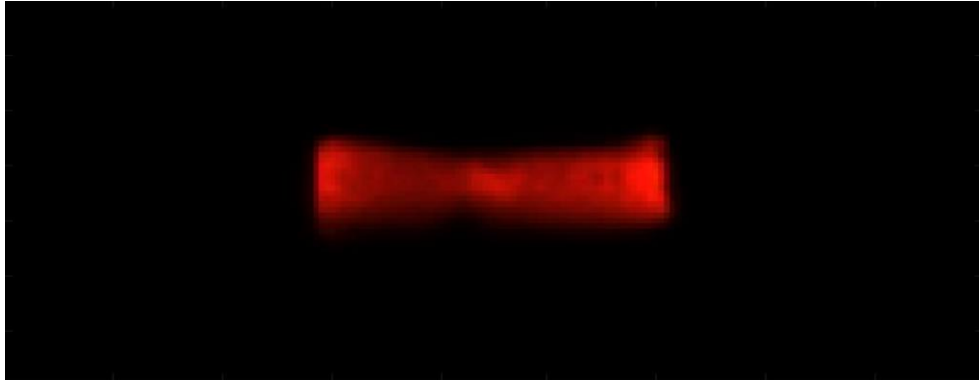
Fig. 3.9. 16-bit TIFF images of burning embers.
(a) Ember 1 – 0.5 m (b) Ember 1 -- 1 m (c) Ember 2 – 0.5 m (d) Ember 2 -- 1 m

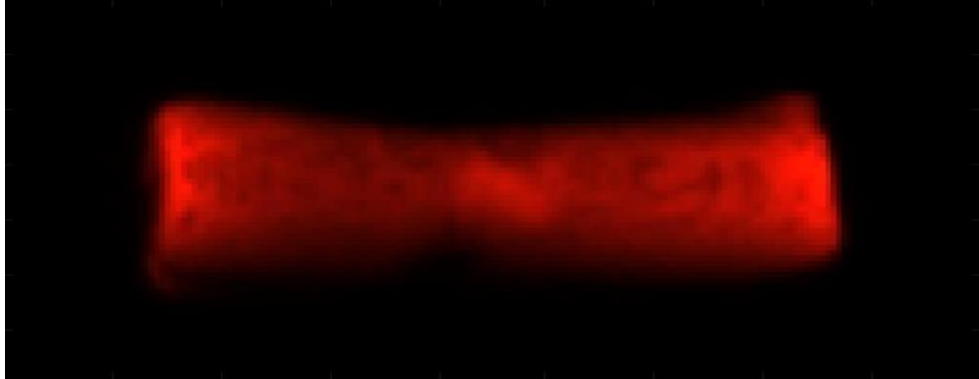Figure 3.10 shows ember temperatures of Ember 1 and Ember 2 at imaging distances of 0.5 and 1 m away from the sample after ratio pyrometry is performed. The G/R curve fits from Fig. 2.6 were used to convert the logarithmic ratio of the normalized green and red pixel values to temperature. The analysis region of both embers was 49 x 162 pixels regardless of imaging distance. There are three stages of smoothing applied to each imaged ember. Figure 3.11 shows each ember after any pixel yielding a temperature outside the range of 600 – 1200 °C or a saturated value are removed. While Camera 2 was only calibrated up to 1100 °C, there is good agreement shown in Fig. 6 between the G/R curves for Camera 1 and Camera 2 at the upper temperatures. Because of this, the Camera 2 ratio pyrometry curve fit was extended to 1200 °C. The exposure time was chosen to keep as many pixels away from saturation as possible. While losing pixels to saturation eliminates hotter areas of the ember, the next shutter speed on the camera after the chosen 0.004 s is 0.002 s. While this would bring the red value of those pixels below saturation, it would further decrease the fit between the ratio pyrometry curve and the lower end of the temperature range. Even at the chosen exposure time of 0.004 s, the lower end of the temperature range is compromised. As mentioned in Section 2.4, the blackbody images chosen to determine the G/R ratio pyrometry fit with temperature use the exposure times that yield the highest possible red pixel values without reaching saturation. At the lower temperatures, this requires exposure times much longer than 0.004 s. Blackbody images of the blackbody surface at 600 °C yield pixel values commensurate with the black null space. Blackbody images of the blackbody surface at 700 °C yield red pixel values around 300. This gap in exposure time causes the lower end of the temperature range to blend in with the black null space.
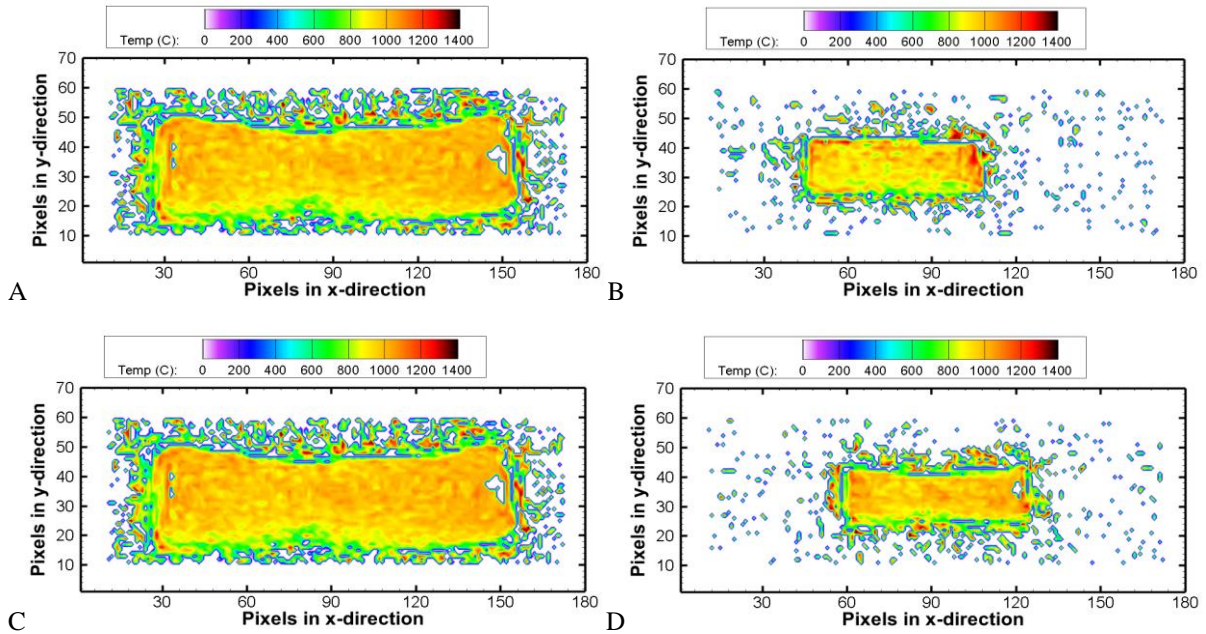
Fig. 3.10. Ember temperatures of embers after G/R ratio pyrometry is completed.
(a) Ember 1 – 0.5 m (b) Ember 1 -- 1 m (c) Ember 2 – 0.5 m (d) Ember 2 -- 1 m
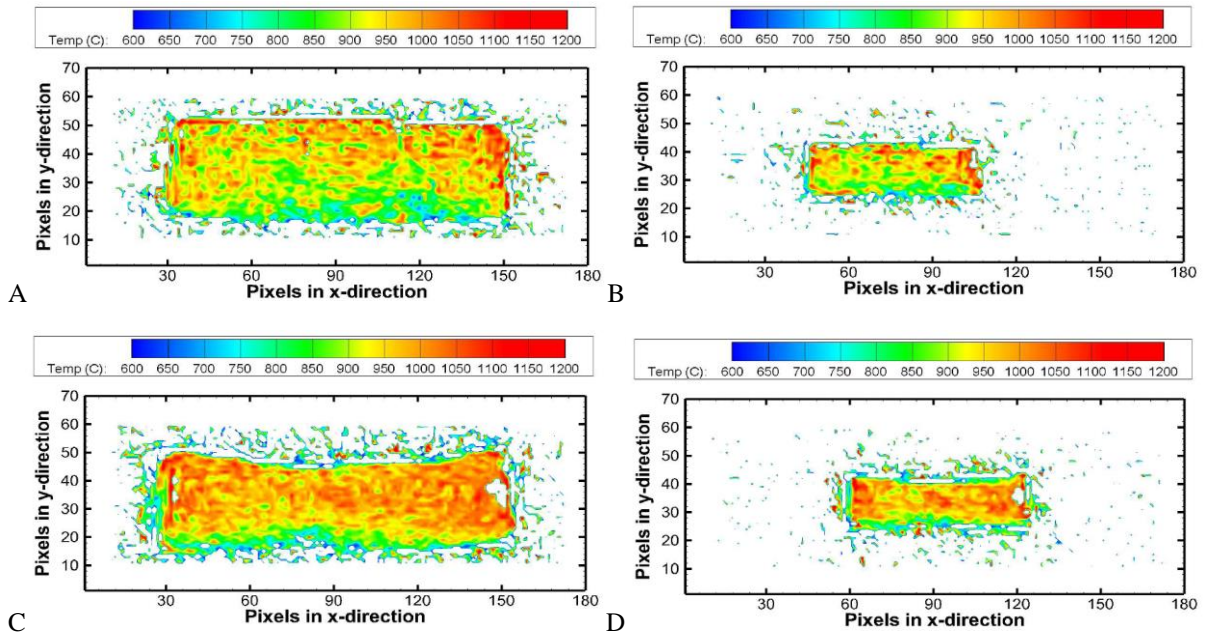
Fig. 3.11. Ember temperatures of embers after eliminating all temperature outside the range of 600-1200 °C.
(a) Ember 1 – 0.5 m (b) Ember 1 -- 1 m (c) Ember 2 – 0.5 m (d) Ember 2 -- 1 m

Fig. 3.12. Ember temperatures of embers after eliminating pixels whose surrounding region do not match the 50% rule.   (a) Ember 1 – 0.5 m (b) Ember 1 -- 1 m (c) Ember 2 – 0.5 m (d) Ember 2 -- 1 m
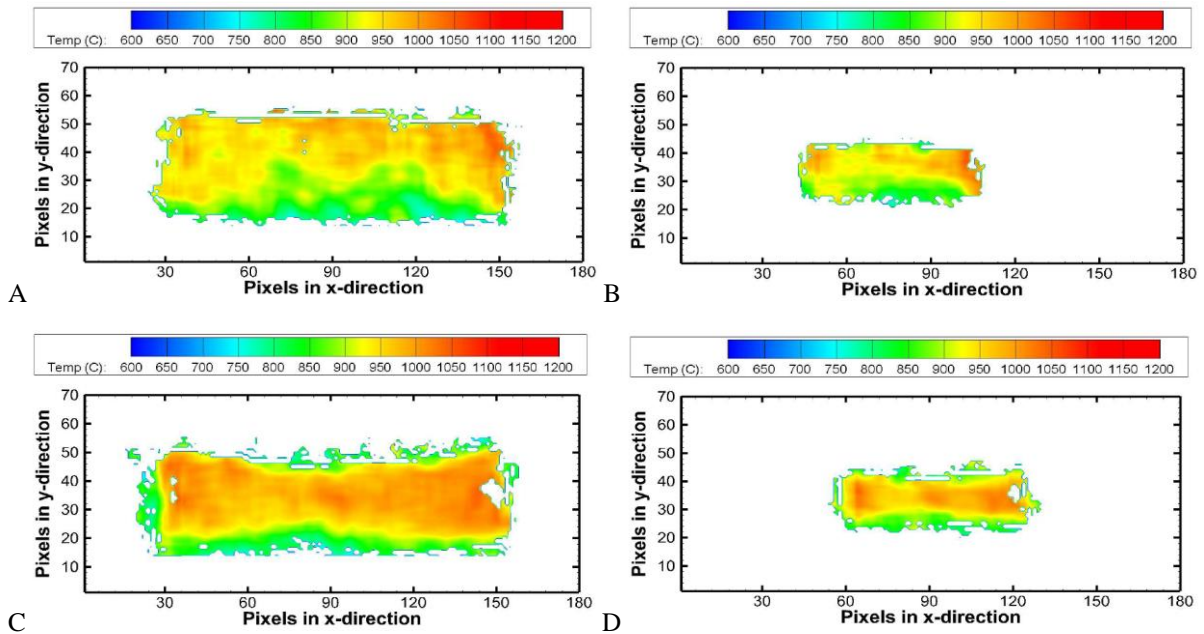
Fig. 3.13. Ember temperatures of embers after averaging the 7 x 7 surrounding region of all remaining pixels. (a) Ember 1 – 0.5 m (b) Ember 1 -- 1 m (c) Ember 2 – 0.5 m (d) Ember 2 -- 1 m

Reference [18] reports an ember surface temperature of around 930 °C, near the upper middle of the temperature range. Since this reported temperature is much higher than the lower end of the temperature range, and the images in Fig. 3.9 match the expected shape of the burning ember, the errors associated with the lower end of the temperature range are ignored and the ratio pyrometry curve fit from Fig. 2.6 is deemed just as valid. After the removal of all pixels outside of the calibration temperature range, about 90% of the pixels in Fig. 3.11 yield temperatures greater than 700 °C, further demonstrating the negligible effects of the lower end of the temperature range. Only 2 pixels were saturated at the 0.5 m distance for Ember 1. No pixels were saturated at the 1 m distance for Ember 1. 45 pixels were saturated at the 0.5 m distance for Ember 2. 13 pixels were saturated at the 1 m distance for Ember 2. Figure 3.12 shows the ember after a null value is assigned to any pixel with more than 24 null pixels in the surrounding 7 x 7 pixel square. Figure 3.13 shows the ember after each remaining pixel is assigned the average temperature of the surrounding 7 x 7 pixel square including itself and excluding any null pixels. Figures 3.14 and 3.15 show the red and green color channel pixel values across Ember 1 and Ember 2, respectively. The temperature distribution across both embers matches the brightness distribution observed in Fig. 3.9. The red and green pixel values follow the same patterns across each ember surface with respect to distance for both Ember 1 and Ember 2. The temperature distribution across both embers is almost identical to the red and green pixel value distributions in Figs. 3.14 and 3.15. The upper surface is hotter than the lower surface of both embers, particularly in Ember 1. This is most likely due to the orientation of the fan with respect to the ember surface. Breaks or gaps in the ember may be associated with pixel saturation, or dark ash disrupting the temperature smoothing across the ember surface.

Fig. 3.14. Color images of the red color channel pixel values across the ember surface.
(a) Ember 1 – 0.5 m (b) Ember 1 -- 1 m (c) Ember 2 – 0.5 m (d) Ember 2 -- 1 m
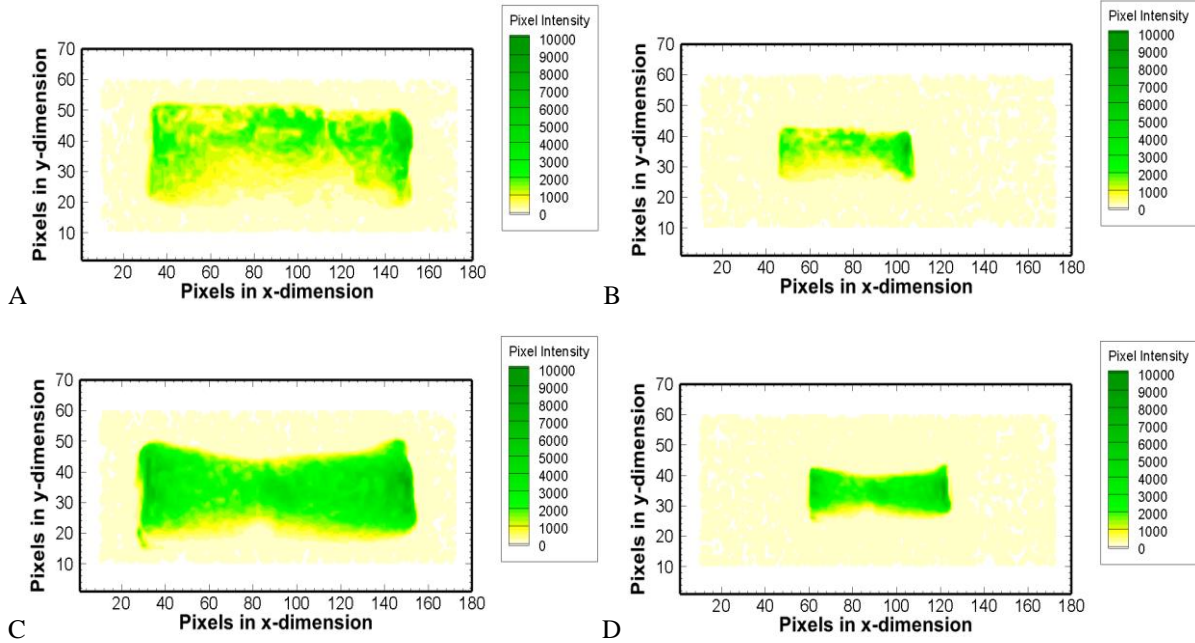
Fig. 3.15. Color images of the green color channel pixel values across the ember surface.
(a) Ember 1 – 0.5 m (b) Ember 1 -- 1 m (c) Ember 2 – 0.5 m (d) Ember 2 -- 1 m

24

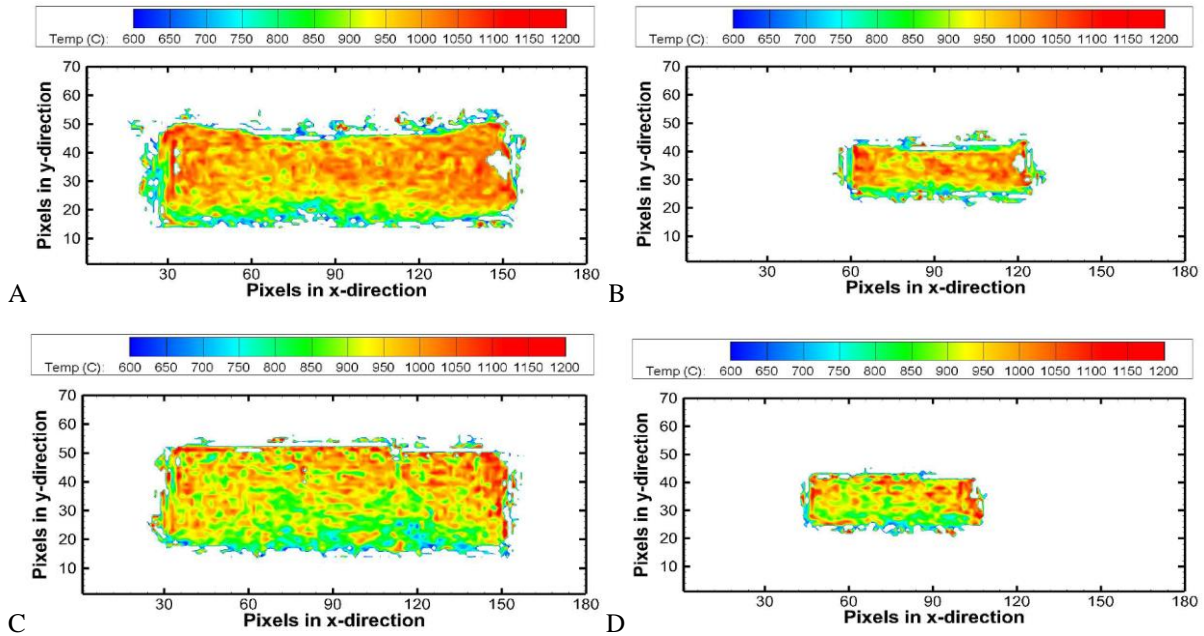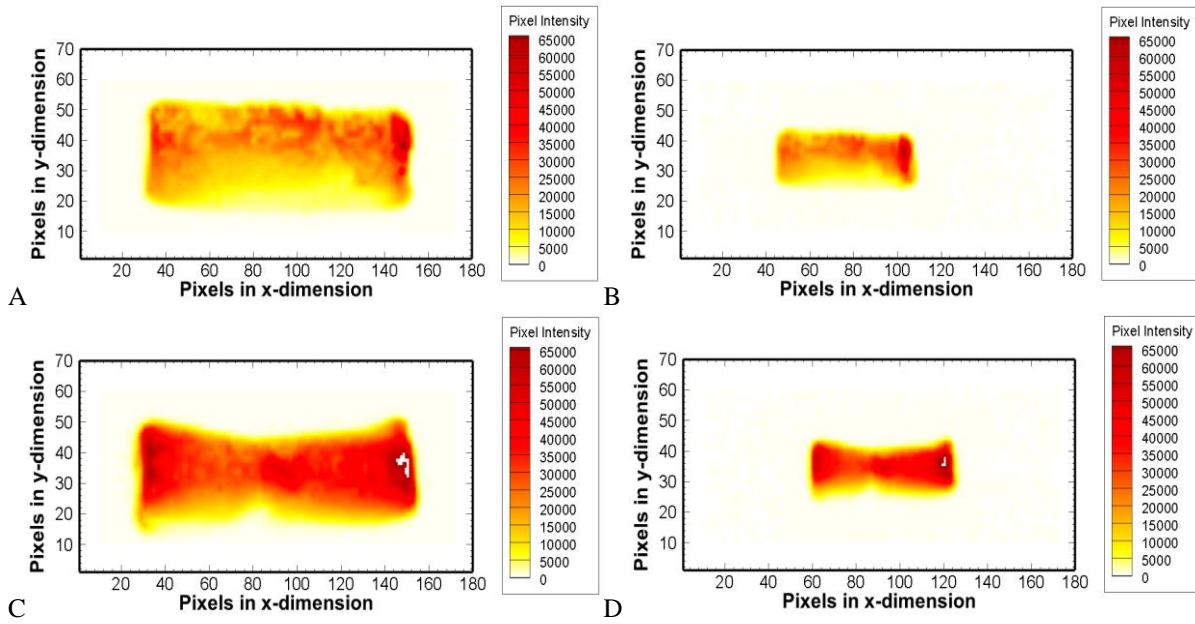The ember temperatures of Ember 1 and Ember 2 have little to no change with respect to distance. The mean temperature of Ember 1 at imaging distances of 0.5 and 1 m using ratio pyrometry after smoothing was calculated with 95% confidence to be 921 ± 1.6 °C and 921 ± 2.9 °C, respectively. The mean temperature of Ember 2 at imaging distances of 0.5 and 1 m using ratio pyrometry after smoothing was calculated with 95% confidence to be 937 ± 2.0 °C and 931 ± 2.8 °C, respectively. There is very good agreement in the mean surface temperature with respect to distance in both Ember 1 and Ember 2.

Figure 3.16 shows ember temperatures of Ember 1 and Ember 2 at imaging distances of 0.5 and 1 m away from the sample after grayscale pyrometry is performed. The curve fits from Fig. 2.7 were used to convert the logarithm of the normalized grayscale pixel values to temperature. The only correction applied to the grayscale pyrometry results was the removal of any pixel yielding a temperature outside the range of 600 – 1200 °C or a saturated value. The results shown in Fig. 3.16 are visibly much less scattered than the results shown in Fig. 3.10. The mean temperature of Ember 1 at imaging distances of 0.5 and 1 m using grayscale pyrometry was calculated with 95% confidence to be 808 ± 2.5 °C and 727 ± 3.8 °C, respectively. The mean temperature of Ember 2 at imaging distances of 0.5 and 1 m using grayscale pyrometry was calculated with 95% confidence to be 820 ± 3.3 °C and 728 ± 3.7 °C, respectively. The mean temperatures provided by grayscale pyrometry change significantly with distance and are quite cooler than the ratio pyrometry temperatures. Grayscale pyrometry is expected to yield cooler temperatures due to the absence of known emissivity and transmissivity values. A major flaw associated with grayscale pyrometry exposed by the analysis of Embers 1 and 2 is the inability to clearly define the border of the ember without manual inspection. A significant number of pixels with a visible location in the black null space surrounding the ember are calculated with grayscale

pyrometry to have a temperature in the 600 – 700 °C range. Manually throwing out every pixel just outside the ember border is simply not a practical or efficient approach for ember pyrometry. A simple method to better estimate the mean temperature of the ember using grayscale pyrometry is to increase the low end of the temperature range used in the calculation from 600 to 700 °C. After this change, the mean temperature of Ember 1 at imaging distances of 0.5 and 1 m using grayscale pyrometry was calculated with 95% confidence to be 864 ± 2.1 °C and 863 ± 3.9 °C, while the mean temperature of Ember 2 at imaging distances of 0.5 and 1 m using grayscale pyrometry was calculated with 95% confidence to be 873 ± 3.4 °C and 869 ± 4.7 °C, respectively. Altering the temperature range provides much better agreement when comparing temperatures between each ember at different distances. Even with the different temperature range, grayscale pyrometry still yields temperatures much cooler than ratio pyrometry, which is expected due to the dependence on the emissivity and transmissivity of the ember surface. The issue with using a temperature range different than the calibration range is the assumption that any pixel with a temperature lower than 700 °C can't exist on the ember. While Refs. [18] and [19] provide ember temperatures above that threshold, no literature provides evidence that spot measurements with resolution to the single pixel level cannot be lower than 700 °C. Because of the lack of clarity regarding the usable pixels in the grayscale temperature calculation, the temperature values reported using grayscale pyrometry are largely ignored.

Figure 3.17 shows ember temperatures of Ember 1 and Ember 2 at imaging distances of 0.5 and 1 m away from the sample after a combination of ratio and grayscale pyrometry is performed. This method of pyrometry was developed by Ref. [18], using the advantages of both ratio and grayscale pyrometry in what they refer to as hybrid pyrometry.

Fig. 3.16. Ember temperatures of embers after grayscale pyrometry is performed.
(a) Ember 1 – 0.5 m (b) Ember 1 -- 1 m (c) Ember 2 – 0.5 m (d) Ember 2 -- 1 m

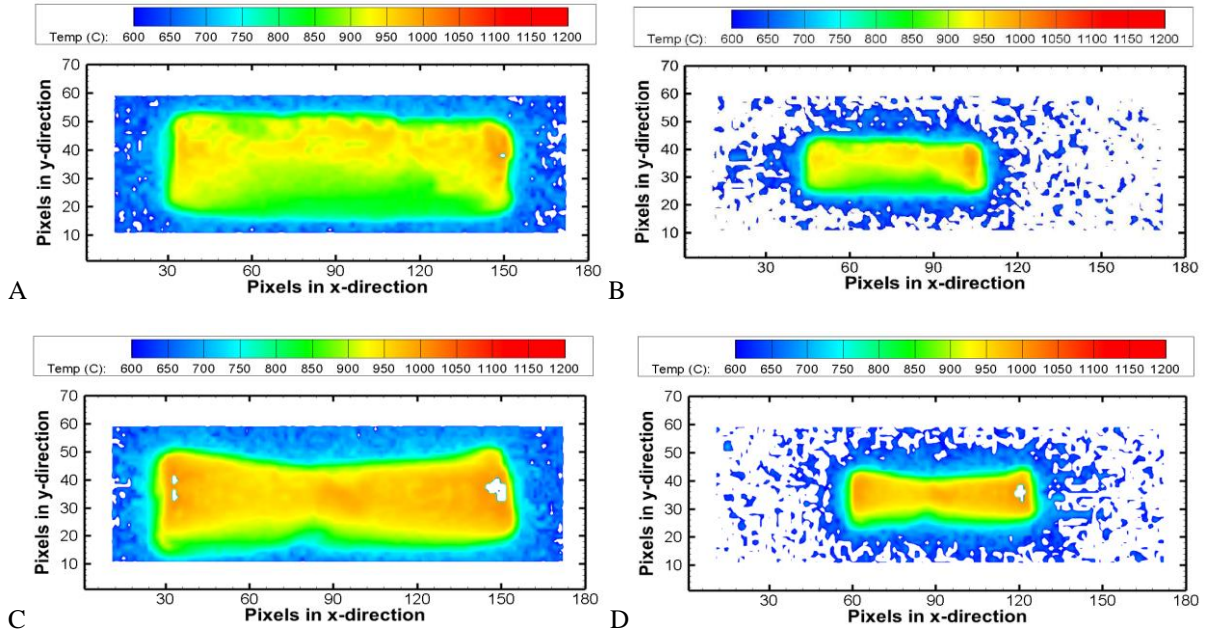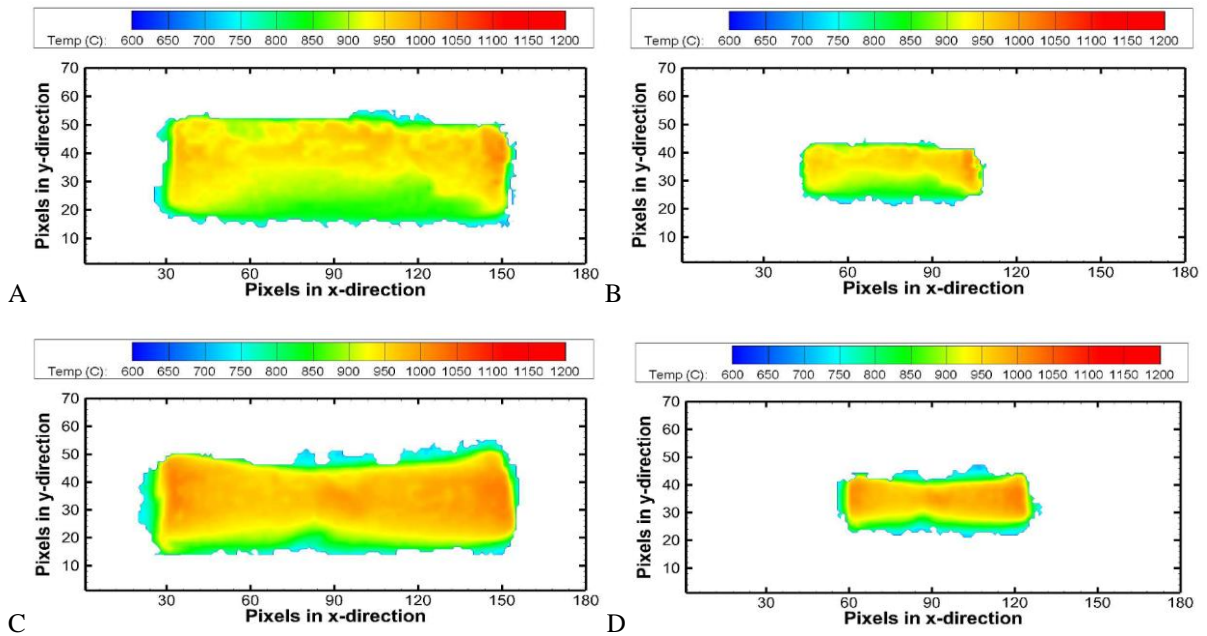Fig. 3.17. Ember temperatures of embers after hybrid pyrometry is performed.
(a) Ember 1 – 0.5 m (b) Ember 1 -- 1 m (c) Ember 2 – 0.5 m (d) Ember 2 -- 1 m

Reference [18] suggests the equation:

$$T_{hybrid} = (T_{GS} + 72.24) / 1.06 , \tag{4}$$

where T_{GS} refers to the grayscale temperature at that specific pixel. Equation 4 allows the low scatter observed in the grayscale results to match the accuracy of the smoothed ratio temperature. Equation 4 was applied to any pixel that had a non-zero temperature value in Fig. 3.13, as well as any empty areas in Fig. 3.13 enclosed by the ember. This allowed Fig. 3.17 to assume the full shape of the observed burning ember. The mean temperature of Ember 1 at imaging distances of 0.5 and 1 m using hybrid pyrometry was calculated with 95% confidence to be 905 ± 1.6 °C and 901 ± 3.3 °C, respectively. The mean temperature of Ember 2 at imaging distances of 0.5 and 1 m using hybrid pyrometry was calculated with 95% confidence to be 923 ± 2.1 °C and 905 ± 4.3 °C, respectively. Similar to ratio pyrometry, the ember temperature has no dependence on distance. The mean temperatures provided by hybrid pyrometry predictably fall just below the comparable ratio pyrometry temperatures. When comparing ratio and hybrid pyrometry, there is less noise observed in Fig. 3.17 across the surface of the ember. However, the uncertainty on the mean temperature reported is slightly larger for hybrid pyrometry. Attempts were made to develop hybrid pyrometry curves similar to Ref. [18] by adjusting the ratio pyrometry temperature to the grayscale pyrometry temperature in isothermal areas of the ember. Due to the quantity of pixels being much lower at the 0.5 and 1 m distances than the embers tested by Ref. [18] at 4.2 cm, no areas are found to be reasonably isothermal on the surfaces of Ember 1 or Ember 2 for ratio and grayscale pyrometry. If the primary motivation of these experiments was to develop an accurate temperature distribution across the surface of an ember, then the results from hybrid pyrometry would be the most reliable. However, with the known accuracy of ratio pyrometry due to no dependence on the surface emissivity or transmissivity combined with the lowest uncertainty on

the mean temperature, the most reliable reported ember temperature comes from ratio pyrometry. The mean temperature of all imaged embers from 0.5 and 1 m using ratio pyrometry was calculated with 95% confidence to be 928 ± 8.0 °C, which shows very good agreement with Ref. [18].
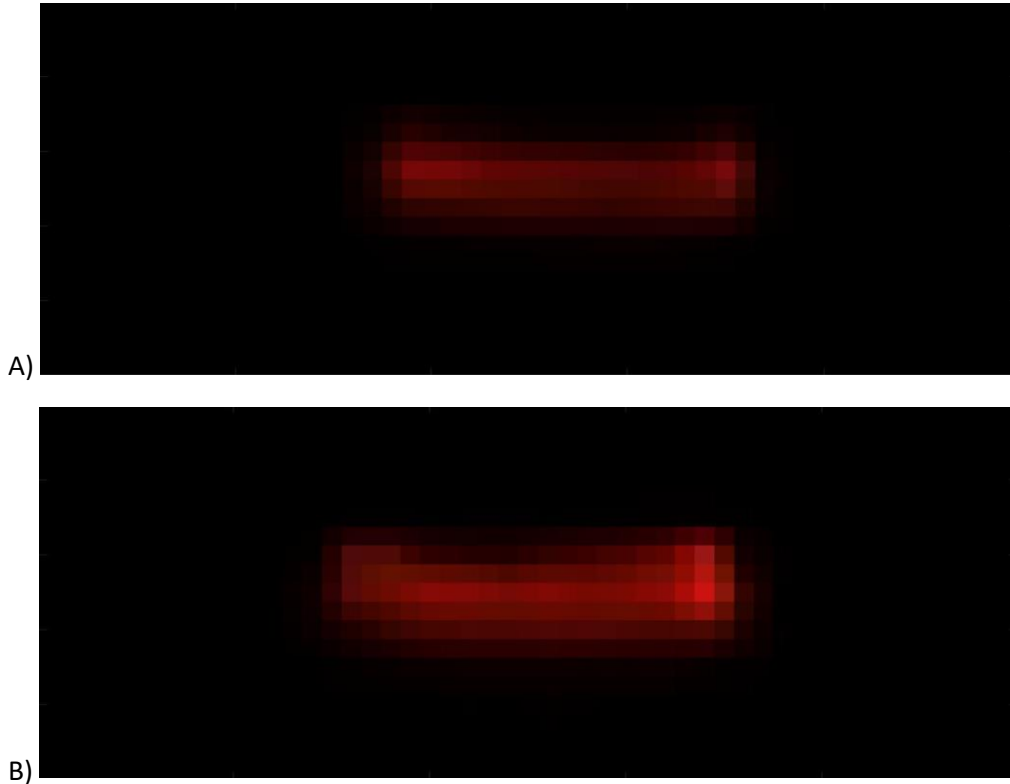
Fig. 3.18. 16-bit TIFF images of burning embers. (a) Ember 3 (b) Ember 4

Figure 3.18 shows Ember 3 and Ember 4 at an imaging distance of 4 m away from the sample. All images in Fig. 3.18 are cropped to a range of 20 x 50 pixels. The original size of each image in Fig. 3.18 was 3672 x 5496 pixels. All images used for pyrometry in this chapter had the same camera properties. The *ISO* was set to 100, the exposure time, *t*, was set to 0.004 seconds, and the f-number, *f*, was set to 2.4. From the 4 m imaging distance, Deformation is difficult to identify due to the size of the image, however both images in Fig. 3.18 appear to show the same ember shape. Similar to Embers 1 and 2, the brightest regions of the ember are the far left and right sides of the sample. Ember 4 appears slightly brighter than Ember 3 across the entire face of the ember.
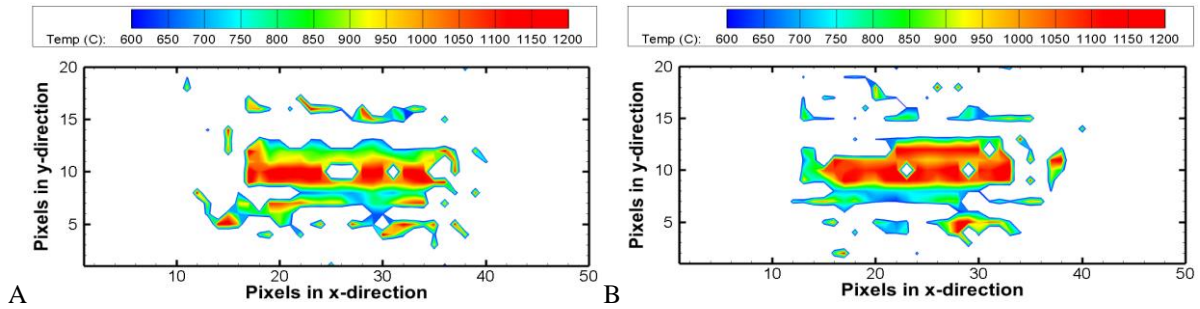
Fig. 3.19. Ember temperatures of embers after ratio pyrometry is performed and all temperatures outside the 600-1200 °C range are removed.   (a) Ember 3 (b) Ember 4

Fig. 3.20. Ember temperatures of embers after temperatures across the ember surface are smoothed.
(a) Ember 3 (b) Ember 4

Fig. 3.21. Color images of the red color channel pixel values across the ember surface.
(a) Ember 3 (b) Ember 4
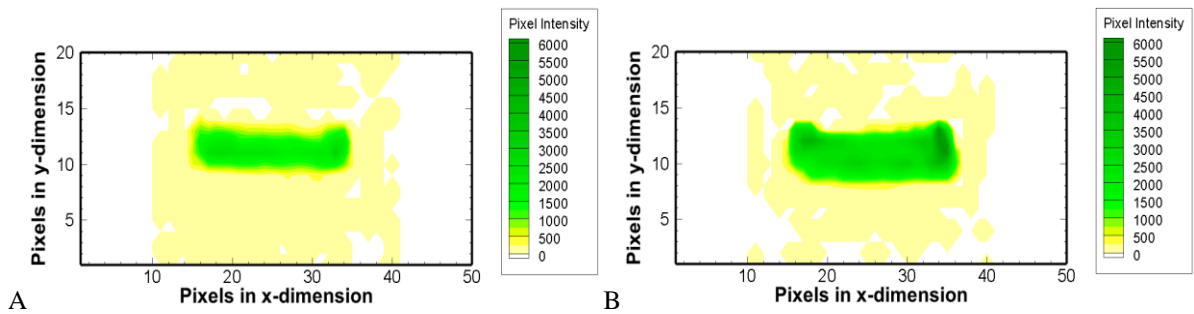
Fig. 3.22. Color images of the green color channel pixel values across the ember surface.
(a) Ember 3 (b) Ember 4

30

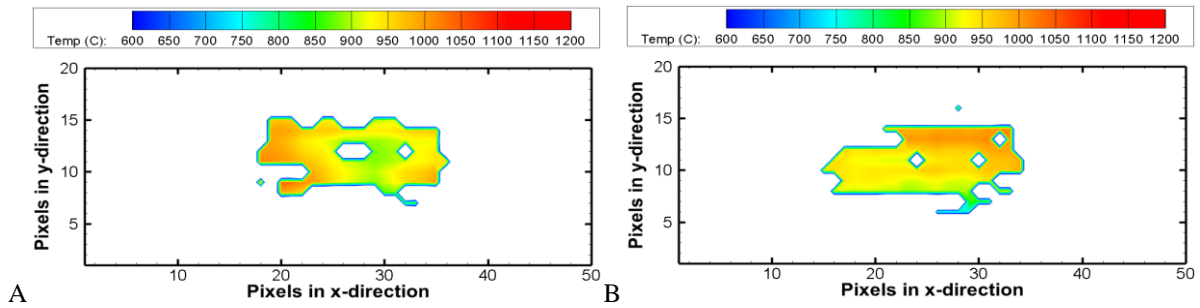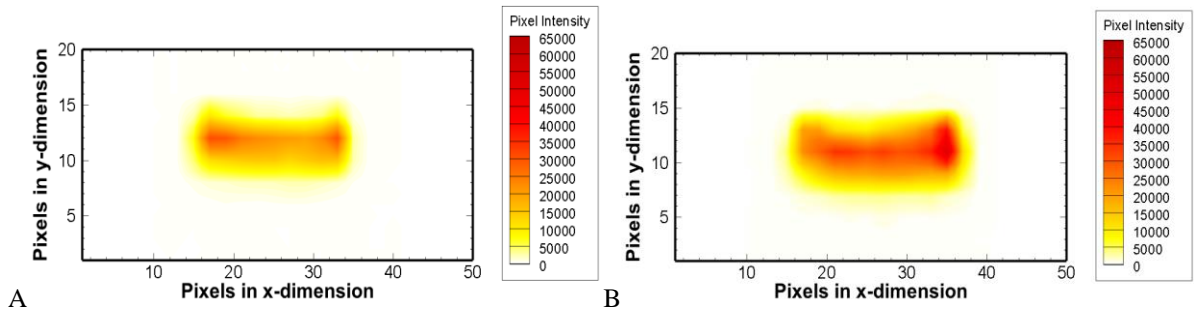Figure 3.19 shows Ember 3 and Ember 4 at an imaging distance of 4 m away from the sample after ratio pyrometry is performed and all temperature outside of the 600-1200 °C range are removed. The original analysis region size of 49 x 162 pixels was cropped for improved visualization of the embers. Figure 3.20 shows Ember 3 and Ember 4 after a null value is assigned to any pixel with more than 24 null pixels in the surrounding 7 x 7 pixel square and each remaining pixel is assigned the average temperature of the surrounding 7 x 7 pixel square including itself and excluding any null pixels. No pixels reached the saturation limit in either Ember 3 or Ember 4. The temperature distributions displayed in Fig. 3.20 have the same patterns across the ember face as the brightness distributions displayed in Fig. 3.18, however the comparison is not as definite as Ember 1 and Ember 2 at both the 0.5 and 1 m distances. While the patterns are alike, there are areas in Fig. 3.20 showing a null area that are clearly part of the ember. These areas cannot be attributed to the removal of saturated pixels, as no pixels reached that mark. These gaps in Fig. 3.20 may be attributed to the loss of pixels due to the G/R ratio fit yielding a temperature outside of the 600-1200 °C temperature range. Embers 3 and 4 lose about 12-13% of their pixels when the temperature range is constrained, while Embers 1-2 lose about 9% at the 2 m distance and 5-6% at the 1 m distance. These percentages come with built in uncertainty due to the location of the lost pixels at the farther imaging distances being more likely to exist in the null space around the ember. The mean temperature of Ember 3 at an imaging distance of 4 m using ratio pyrometry after smoothing was calculated with 95% confidence to be 944 ± 7.5 °C. The mean temperature of Ember 4 at an imaging distance of 4 m using ratio pyrometry after smoothing was calculated with 95% confidence to be 944 ± 8.8 °C. There is very good agreement in the mean surface temperature with respect to distance in both Ember 3 and Ember 4. Embers 3 and 4 are calculated to have slightly larger temperature than Embers 1 and 2. While slight variation is observed, the 95%

31

confidence intervals of Embers 1 and 2 overlaps the same interval for Embers 3 and 4. When observing Figs. 3.21 and 3.22, the red and green pixel values across the ember surface follow very similar patterns. When comparing Figs. 3.21 and 3.22 to Fig. 3.14 and 3.15, the red and green pixel values are consistently lower across Embers 3 and 4 than Embers 1 and 2. Ratio pyrometry on Embers 3 and 4 still yield temperatures in the range of Embers 1 and 2 even with the lower pixel values. The mean surface temperature across the 0.5, 1, and 4 m imaging distances was calculated with 95% confidence to be 928 ± 9.1 °C.

Chapter 4: Ember Temperatures with Different Illuminations

4.1. Introduction

This chapter demonstrates the application of ratio pyrometry to a burning ember with an applied light source. The ability to identify ember surface temperature in the presence of an applied light source would allow the chosen pyrometer to be used in imaging conditions outside of a controlled laboratory environment. A series of four images is taken for each tested ember from a 1 m distance. Each image has a unique combination of the light source being turned on and off and the image background being white or black. The relationship between illuminance on the ember surface and background color with surface temperature are both observed and quantified.

4.2. Experimental

The experimental setup for this chapter very closely resembles Fig. 3.2, with the only change being the removal of the front camera. Figure 4.1 shows a diagram of the experimental setup of all imaging performed in Chapter 4. The generation, mounting, and ignition arrangement for each
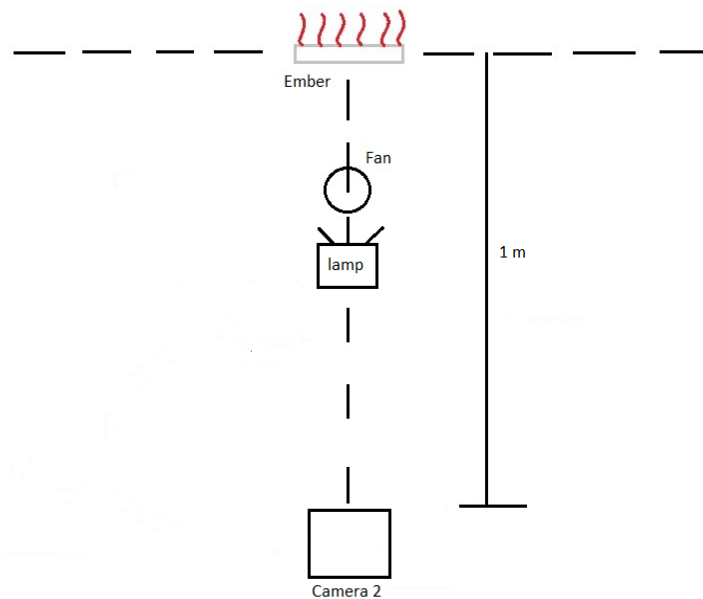

Fig. 4.1. Diagram of the experimental setup for imaging at 2 meters with varying illumination and background.

33

wooden dowel sample tested in Chapter 4 is identical to that of Chapter 3. Camera 2 was kept at the 1 m distance similar to Chapter 3, however for these experiments only one camera was used. The white background and handheld fan from Chapter 3 were kept in the same place and used again. The black background was modeled with a black curtain draped in front of the white sheets of paper. The curtain was mounted with a long wire and a zip tie, allowing free range of motion behind the ember. In some experiments, the fluorescent lights in the testing laboratory were used as the light source. When the room lights were not used, a Dolan-Jenner Fiber-Lite Series 180 tungsten lamp was used. The lamp was placed as far away from the ember as possible without infringing on the camera view of the mounted sample. The lamp was positioned on the lab table in such a manner that if a vertical slice was taken through the center of the light source, the middle of the sample would lie in that sample plane. The front edge of the lamp was raised off the table to the point that allowed a direct line of sight between the aperture of the light source and the front surface of the ember. A Dr. Meter digital lux light meter with a range of 0.1 – 200,000 lux range was used to measure the intensity of light hitting the ember surface.

4.3. Procedures

Before ignition, the focus of both cameras is set on the face of the sample. The focus is set with the camera zoomed all the way out and the laboratory lights on. The desired luminous flux provided by the light source is calibrated before ignition with the light meter by angling it towards the aperture of the light source directly in front of the sample surface. The light meter was set to measure in units of lux, which is the SI unit of illumination [26]. Ignition is achieved by moving the flame tip of the butane light across the base of the sample until uniform burning is observed. After the ember transfers from flaming combustion to smoldering, the fan was activated to aid uniform smoldering, similar to Chapter 3. For each tested ember, four images are taken. The first

image is taken with no light source and a black/white background. The second image is taken with the light source applied and the same background as the first image. Between the second and third image, the original background is pulled out of the camera view, revealing the white/black background, depending on what background was used first. The third image is then taken with the light source applied and the next background. Lastly, the fourth image is taken with no applied light source and the same background as the third image. The order of background color was changed between the experiments in which Ember 5 and Ember 6 was imaged. The first image is taken roughly 5-10 seconds after the fan is triggered. The images are taken in intervals of about 2 seconds, allowing the light source to settle or the background to be altered. Images were taken in the RAW format and converted to 16-bit TIFF files using the same process laid out in section 2.3. The red, green, and blue values of each pixel were determined using MATLAB. Excel and MATLAB were both used to analyze each ember.

4.4. Results

Figures 4.2 and 4.3 show each sequence of four images for Ember 5 and Ember 6 at an imaging distance of 1 m away from the sample. All images in Figs. 4.2 and 4.3 are cropped to a range of 70 x 180 pixels. The original size of each image in Figs. 4.2 and 4.3 was 3672 x 5496 pixels. All images used for pyrometry in this chapter had the same camera properties. The *ISO* was set to 100, the exposure time, t, was set to 0.004 seconds, and the f-number, f, was set to 2.4. Without any external illumination applied, the only visible areas in the image are the glowing parts of the ember. With an applied light source, the black burned areas of the ember become much more apparent. The images in Figs. 4.2 and 4.3 with no applied illumination have a similar appearance to the naked eye as Fig. 3.9. Both embers show a similar deformation pattern, with the middle of the ember pinching in the y-direction. Both embers are visibly brightest on the ends of the sample.

The ends of Ember 5 are visibly more pronounced than the middle of the surface, while Ember 6 shows a slightly more even distribution of brightness across the sample. Each image in Fig. 4.2 shows a similar pattern. The last image in Fig. 4.3 shows the ember start to break in the middle, with the left side of the ember surface appearing dimmer than the comparable area in the preceding three images.
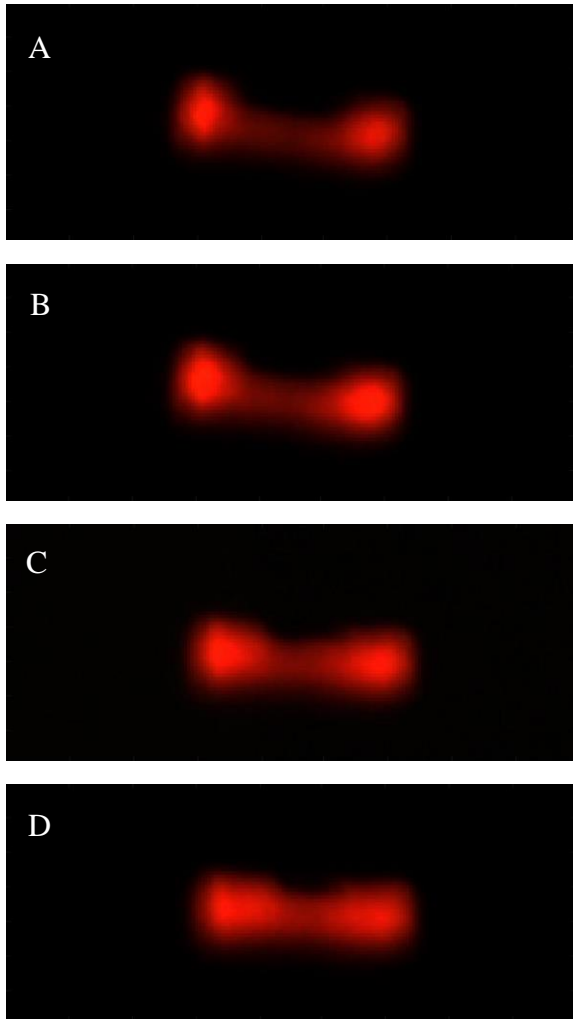

Fig. 4.2. 16-bit TIFF images of Ember 5
(a) Lights Off & Black Background
(b) Lights On & Black Background
(c) Lights On & White Background
(d) Lights Off & White Background
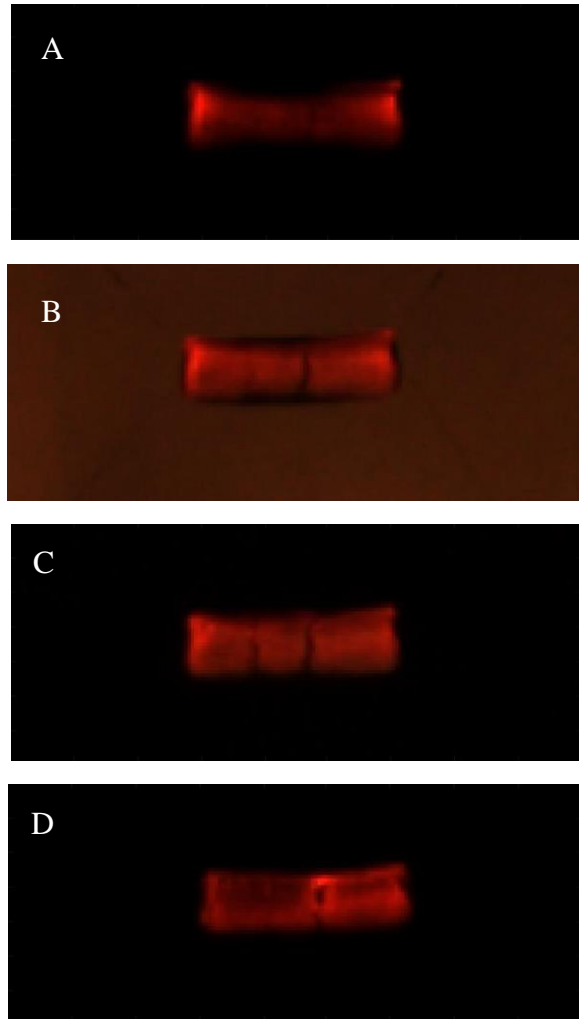
Fig. 4.3. 16-bit TIFF images of Ember 6
(a) Lamp Off & White Background
(b) Lamp On & White Background
(c) Lamp On & Black Background
(d) Lamp Off & Black Background

The light source used for the illuminated test conditions with Ember 5 was the fluorescent lights of the testing laboratory. The luminous flux received by the ember surface facing the camera was between 50-300 lux, depending on the specific angle of the light meter. This amount of luminous flux is comparable to the light level of a very dark day [29]. The unobstructed luminous flux measured by the light meter from the laboratory lights is around 1000 lux. Due to the placement of the sample on the laboratory table, the general line of sight between the sample and the lights is impeded by immovable objects. The light source used for the illuminated test conditions with Ember 6 was the tungsten lamp. The luminous flux received by the ember surface facing the camera was about 2500 lux. This amount of luminous flux is slightly larger than the light level of an overcast day [29]. Due to the placement of the lamp, the light meter reading for Ember 6 was more consistent at the sample surface facing the camera than that of Ember 5.

Figure 4.4 shows ember temperatures of Ember 5 for each background and lighting configuration. The ember temperatures in Fig. 4.4 represent Ember 5 after ratio pyrometry has been performed. Temperature smoothing steps performed but not illustrated include applying the G/R curve fits from Fig. 2.6, removing all temperatures outside the range of 600-1200 °C, and removing any pixels without at least 50% of the surrounding 7 x 7 region's pixels having nonzero temperatures. The ember temperatures in Fig. 4.4 are the result of taking the average temperature of each remaining nonzero pixel's 7 x 7 surrounding region, ignoring any nonzero pixels in that average. Saturated pixels were removed before ratio pyrometry was performed. In the order of Fig. 4.4a to Fig. 4.4d, Ember 5 had 24, 111, 50, and 11 saturated pixels. The images with illuminated test conditions have more saturated pixels than those without light applied, however this may be attributed to random fluctuation in the smoldering surface of the ember. The temperature distributions in Figs. 4.4a and 4.4d show similar patterns to the comparable brightness distribution

in Fig. 4.2. The mean temperature of Ember 5 without illumination and a black background is 923 ± 4.2 °C. The mean temperature of Ember 5 without illumination and a white background is 926 ± 3.7 °C. The temperature distribution displayed in Fig. 4.4b is close to matching those in Figs.
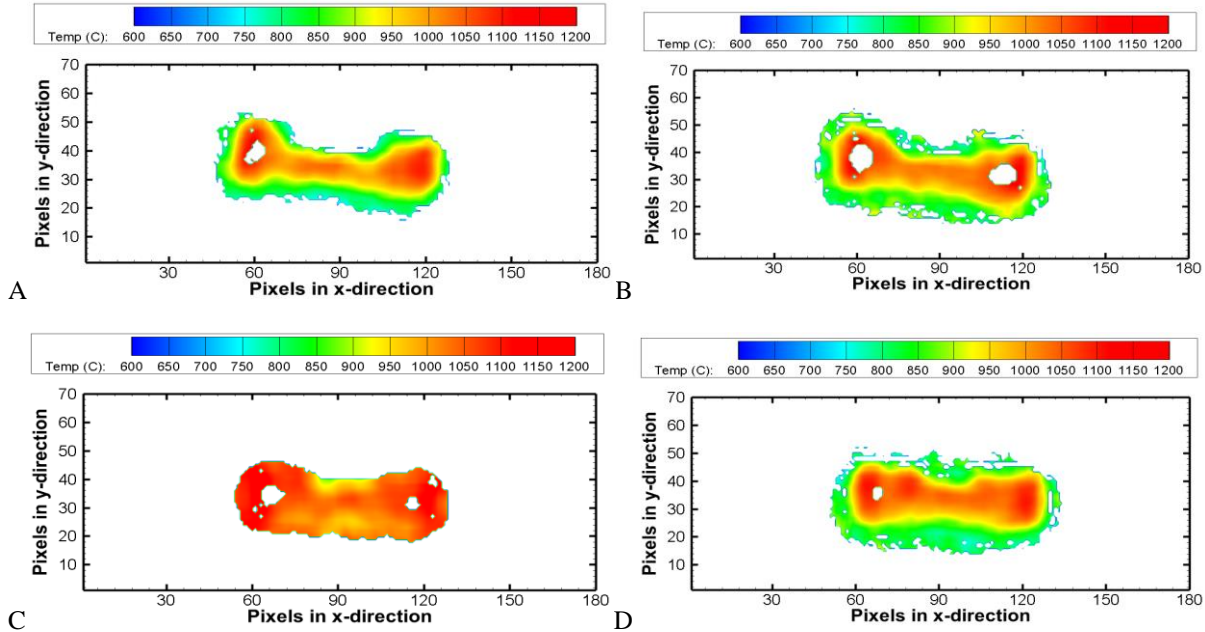
Fig. 4.4. Ember temperatures of Ember 5 after ratio pyrometry is performed, all temperatures outside the 600-1200 °C range are removed, and temperatures across the surface are smoothed.
(a) Lights Off & Black Background (b) Lights On & Black Background (c) Lights On & White Background
(d) Lights Off & White Background

4.4a and 4.4d, except for additional saturated pixels on the left and right ends of the ember. Fig. 4.4c is notably missing the cool outer border of the ember, with a similar shape in the hot inner middle region of the ember to Fig. 4.4b. The mean temperature of Ember 5 with illumination and a black background is 932 ± 3.4 °C. The mean temperature of Ember 5 with illumination and a white background is 1047 ± 2.4 °C. In test configurations with no added illumination, Ember 5 shows little to no difference in mean temperature or temperature distribution when the background base color is changed. In test configurations with a present light source, Ember 5 shows a large difference in mean temperature when the background base color is changed. When the background color remains constant and illumination is added, there is a noticeable increase in the mean

temperature, especially between Figs. 4.4c and 4.4d with a white background. Figures 4.5 and 4.6 show the individual red and green color channel values across the surface of Ember 5. When comparing the red pixel distributions of each image in Fig. 4.5, the only noticeable differences are the increase in red pixel values surrounding the ember in Fig. 4.5c, as well as the empty pockets attributed to the removal of saturated pixels. No appreciable increases are seen in the red pixel values across the ember surface are seen when illumination is added. When observing the green pixel values in Fig. 4.6, the presence of illumination is viewed to have a greater impact on the pixel values across the ember surface. The primary difference between Fig. 4.5 and Fig. 4.6 is that the green pixel values in the surrounding area of Fig. 4.6c are very similar to those around the border of the ember surface in the unilluminated images, whereas the rise in red pixel values around the ember in Fig. 4.5c are much lower than the ember surface pixel values in the unilluminated images. Pixels on the ember without illumination with either black or white backgrounds are viewed to rise to a certain green pixel value threshold around 700 when the light source is added. This threshold value is close to the green pixel values seen in the area surrounding the ember in Fig. 4.6c. Pixels on the ember that were already at or above this threshold do not experience any value change in the presence of illumination, remaining close to the unilluminated value. Because of this, the only valid G/R ratios observed in Fig. 4.4c come in the hot middle region of the ember, where the green pixel values show no change in the presence of illumination. Changes in background color do not contribute to any changes across the ember surface for Ember 5. When the 300 lux light source is applied to Ember 5, increases viewed in the green pixel channel disrupt ratio pyrometry at cooler areas around the edge of the ember.

Fig. 4.5. Color images of the red color channel pixel values across surface of Ember 5.
(a) Lights Off & Black Background (b) Lights On & Black Background (c) Lights On & White Background
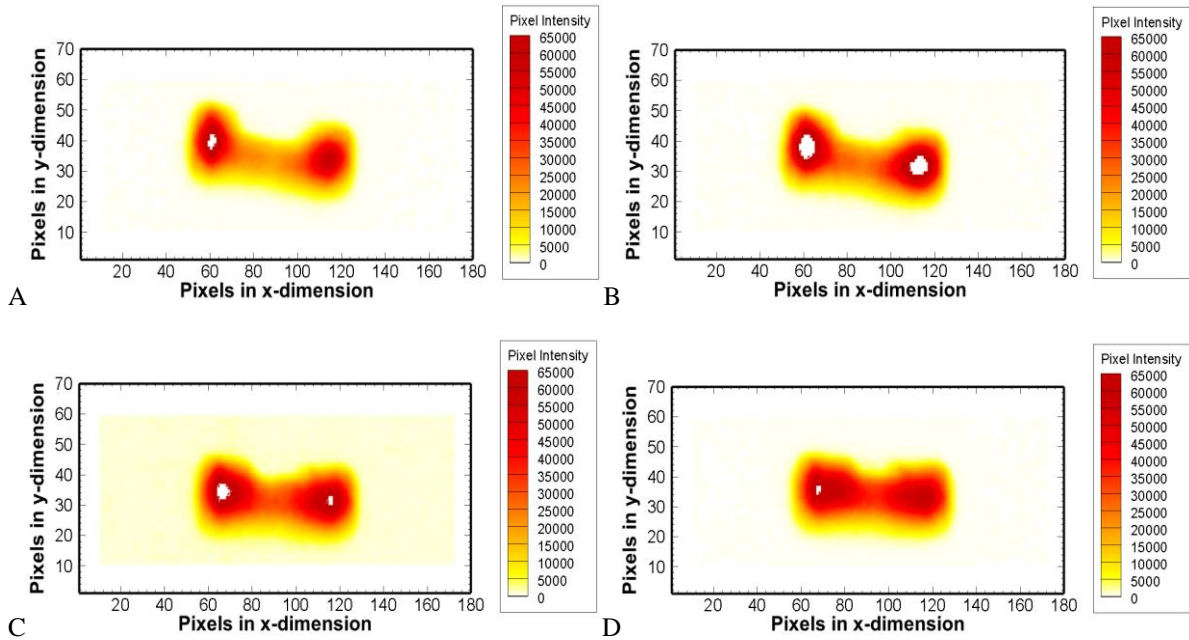(d) Lights Off & White Background

Fig. 4.6. Color images of the green color channel pixel values across surface of Ember 5.
(a) Lights Off & Black Background (b) Lights On & Black Background (c) Lights On & White Background
(d) Lights Off & White Background

Figure 4.7 shows ember temperatures of Ember 6 for each background and lighting configuration. The ember temperatures in Fig. 4.7 represent Ember 6 after ratio pyrometry and temperature smoothing have been performed, analogous to Fig. 3.13. No saturated pixels were found in images taken with illumination. Only 3 saturated pixels were found in the images taken without illumination. This confirms the patterns of saturated pixels observed with Ember 5 being caused predominantly by random fluctuations on the ember surface. The temperature distributions in Figs. 4.7a and 4.7d show similar patterns to the comparable brightness distribution in Fig. 4.3. The mean temperature of Ember 6 without illumination and a white background is 909 ± 2.5 °C. The mean temperature of Ember 6 without illumination and a black background is 933 ± 2.3 °C. The agreement between temperature distributions and mean temperatures across the unilluminated cases is not the best, however this is expected due to the clear differences in brightness across the ember surface in Figs. 4.3a and 4.3d.
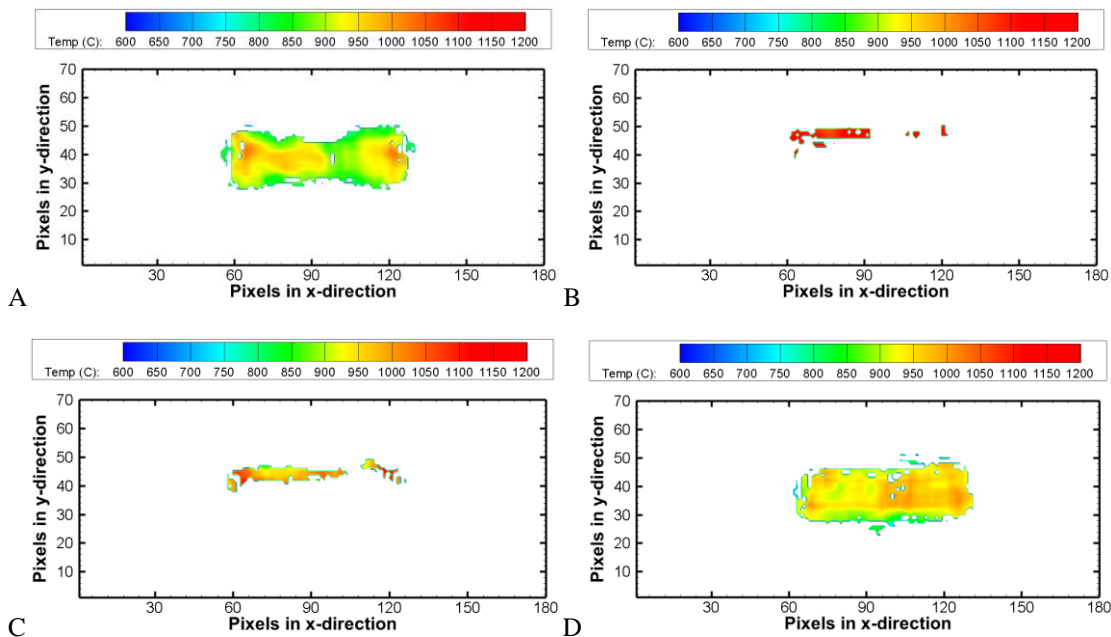
Fig. 4.7. Ember temperatures of Ember 6 after ratio pyrometry is performed, all temperatures outside the 600-1200 °C range are removed, and temperatures across the surface are smoothed.
(a) Lamp Off & White Background (b) Lamp On & White Background (c) Lamp On & Black Background
(d) Lamp Off & Black Background
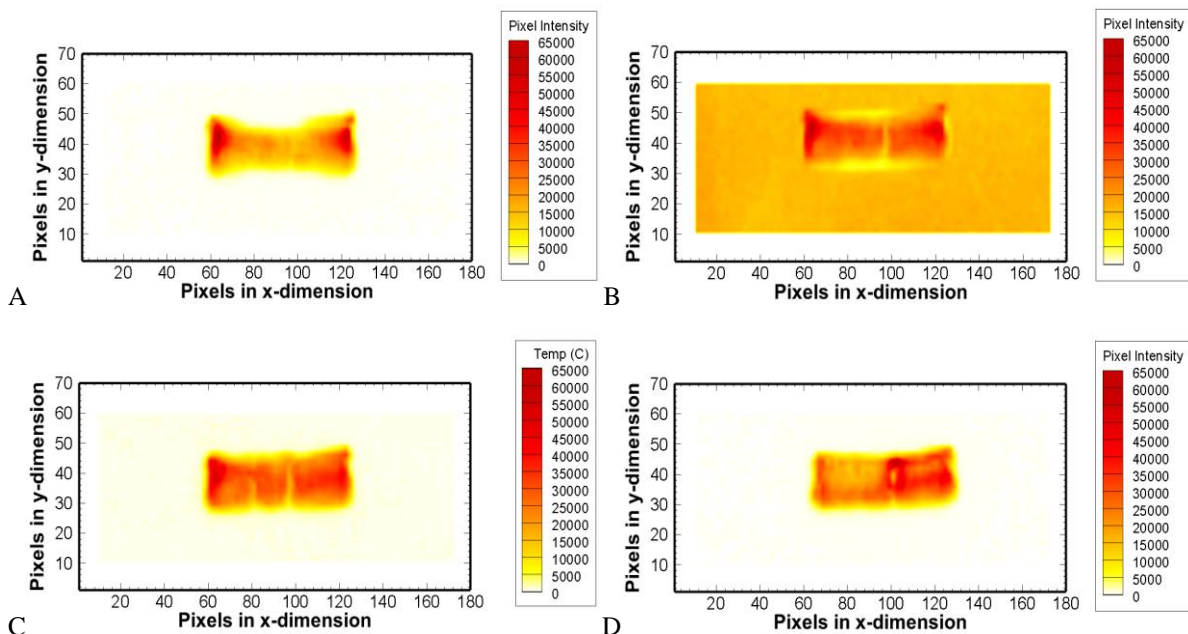
Fig. 4.8. Color images of the red color channel pixel values across surface of Ember 6.
(a) Lamp Off & White Background (b) Lamp On & White Background (c) Lamp On & Black Background
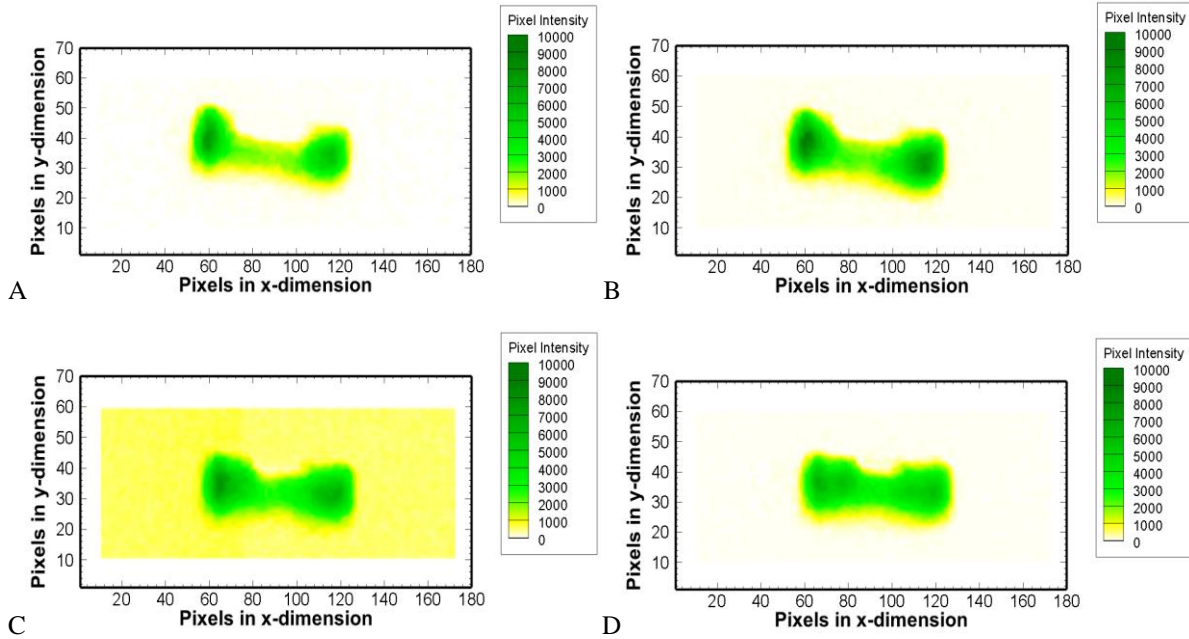(d) Lamp Off & Black Background
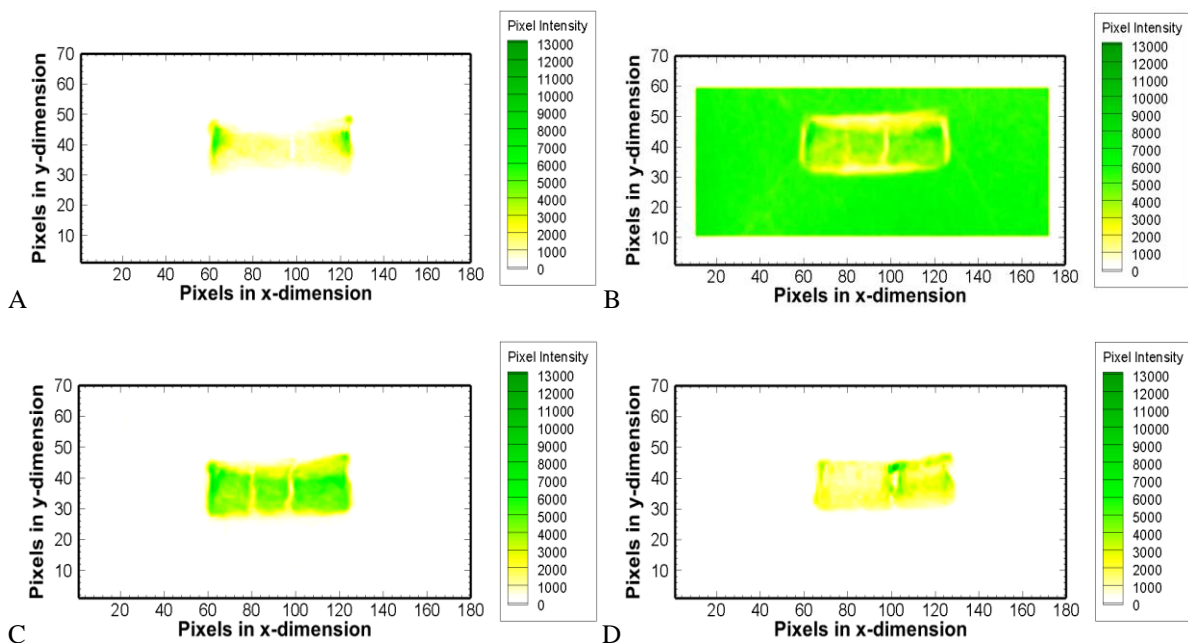
Fig. 4.9. Color images of the green color channel pixel values across surface of Ember 6.
(a) Lamp Off & White Background (b) Lamp On & White Background (c) Lamp On & Black Background
(d) Lamp Off & Black Background

The temperature distributions shown in Figs. 4.7b and 4.7c do not match the comparable brightness distributions, with only the upper region of the ember yielding usable temperature values. When comparing just this upper region to the temperature distributions of the unilluminated images, the temperatures appear to also be quite higher. Figures 4.8 and 4.9 show the individual red and green color channel values across the surface of Ember 6. The trends observed in the red pixel channel across Ember 6 are like those observed in Ember 5. The red pixel channel behaves similarly to the brightness distribution of the ember. The area surrounding the ember in Fig. 4.8b has a much higher red pixel value than the other three images, however the red pixel values across the ember surface are still consistently higher than the surrounding area. There is little change observed in the red pixel channel values between the unilluminated and illuminated images across the surface of Ember 6, similar to Ember 5.When illumination is added to Ember 6, the green pixel values across the ember surface are observed to increase similar to Ember 5. The primary difference between Ember 5 and Ember 6 is the increase viewed in the green color channel is much larger for Ember 6, reaching pixel values around 5500 across the ember surface. While the green pixel values across the surface of Ember 5 were only observed to change around the ember border, the green pixel values across the surface of Ember 6 are observed to change across nearly the entire surface. When comparing Figs. 4.9a and 4.9d with Figs. 4.9b and 4.9c, it is clear that the green pixel intensities across the ember surface rise across nearly the entire ember surface to the threshold value of about 5500. This threshold value is once again observed to be nearly equal to the green pixel value of the null space in the case of the white background with illumination. Changes in background color do not contribute to any changes across the ember surface for Ember 6. Images with no illumination have mean temperatures that show very good agreement with Embers 1-4 as well as Ref. [18]. The mean surface temperature across all imaging distances with no illumination is

calculated to be 931 ± 6.2 °C. When the 2500 lux light source is applied to Ember 6, increases viewed in the green pixel channel disrupt ratio pyrometry across most of the ember. There is a clear increase in the disruption of ratio pyrometry as the luminous flux applied to the ember is increased. If luminous flux were increased to levels matching full daylight, which Ref. [29] suggests is near 11000, ratio pyrometry would likely be impossible at the used camera properties. Due to disruptions in ratio pyrometry present upon the addition of illumination to the testing environment, the G/R curve fit developed in Fig. 2.6. is limited in its scope of applicability. The inability to function in the presence of light limits the chosen pyrometer to a controlled laboratory environment with no present light sources.

Chapter 5: Conclusions and Future Work

Ember surface temperature was calculated using two-color ratio, grayscale, and hybrid pyrometry. Pyrometry was verified to be applicable with normalized color pixel values opposed to a more traditional usage of spectral intensities. Two different Sony DSC-RX10 III cameras were for ratio and grayscale pyrometry with a blackbody furnace with the range of 600 – 1200 °C, yielding curves relating surface temperature to normalized color pixel values. Pixel values were normalized to account for differences in imaging camera settings. Signal to noise ratios of around 850 and 46 for grayscale and ratio pyrometry were obtained. Embers were imaged at 0.5 and 1 m distances simultaneously with no added illumination. A shutter triggering system was developed to take images with both cameras of the same ember within 10 ms of one another. Embers were imaged at a 4 m distance with no added illumination. The mean surface temperature across the 0.5, 1, and 4 m imaging distances using the normalized G/R pixel value ratio was calculated with 95% confidence to be 931 ± 6.2 °C. Ember surface temperature was determined to be independent of imaging distance with no added illumination. Due to uncertainty related to the physical ember location in each image, grayscale pyrometry temperature results were deemed unreliable. Attempts to replicate the hybrid pyrometry method of Ref. [18] were unsuccessful due to insufficient pixel counts, leaving no regions of the ember able to be modeled as isothermal. Embers were imaged at a 2 m distance with varying illumination and background color. Luminous fluxes of around 150 and 2500 lux were both used. Background color was observed to have no effect on ember temperature with no illumination. The disruption of ratio pyrometry was observed to increase as the luminous flux was increased. Disruption was caused by lopsided increases in the green pixel values when compared to the red pixel values. While the inability to perform in the presence of an applied light source does prevent the pyrometer from functioning in the outdoors, the ratio

pyrometer was observed to yield repeatable surface temperature values within a 95% confidence interval across all imaging distances with no illumination.

Future work with ember pyrometry should immediately focus on imaging with added illumination. New blackbody calibrations are recommended in the presence of illumination, as well as the possible introduction of optical instrumentation to address the unequal rise in green pixel values in the presence of added illumination. Simultaneous imaging at a constant distance with variable exposure times is recommended to possibly enhance the reliability of the calibrated temperature range. Imaging should be tested with some capacity of a variable background comparable to an outdoor setting. Ratio pyrometry should be applied to moving embers and clumps of embers in various formations. Attempts should be made to identify the emissivity of a wood ember, as well as the effects of increased smoke obscuration between camera and ember. Lastly, imaging should be taken from distances of 8 meters and beyond to verify the conclusions of this thesis.

References

[1]   Mell, William, et al. "The Wildland-Urban Interface Fire Problem – Current Approaches and Research Needs." *International Journal of Wildland Fire*, vol. 19, no. 2, Jan. 2010, doi:10.1071/WF07131.

[2]   Hill, Alice, and Madeline Babin. "Why U.S. Wildfires Will Only Get Worse." *Council on Foreign Relations*, Council on Foreign Relations, 16 Sept. 2020, www.cfr.org/in-brief/us-wildfires-california-oregon-climate-change-worse.

[3]   "CAL FIRE Investigators Determine Cause of the Camp Fire." *CAL Fire*, California Department of Forestry and Fire Protection , 15 May 2019, www.fire.ca.gov/media/5121/campfire_cause.pdf.

[4]   "Top 20 Most Destructive California Wildfires." *CAL Fire*, Nov. 2020, www.fire.ca.gov/media/11417/top20_destruction.pdf.

[5]   Suzuki, Sayaka, et al. "Role of Firebrand Combustion in Large Outdoor Fire Spread." *Progress in Energy and Combustion Science*, vol. 76, Jan. 2020, doi:https://doi.org/10.1016/j.pecs.2019.100801.

[6]   "Spotting Fire Behavior." *NWCG*, 9 Apr. 2019, www.nwcg.gov/publications/pms437/crown-fire/spotting-fire-behavior.

[7]   Urban, James, et al. "Smoldering Spot Ignition of Natural Fuels by a Hot Metal Particle." *Proceedings of the Combustion Institute*, vol. 36, no. 2, 2017, pp. 3211–3218., doi:https://doi.org/10.1016/j.proci.2016.09.014.

[8]   Caton, S.E., Hakes, R.S.P., Gorham, D.J. et al. Review of Pathways for Building Fire Spread in the Wildland Urban Interface Part I: Exposure Conditions. Fire Technol 53, 429–473 (2017). https://doi.org/10.1007/s10694-016-0589-z

[9]   Zhou, K., Suzuki, S. & Manzello, S.L. Experimental Study of Firebrand Transport. Fire Technol 51, 785–799 (2015). https://doi.org/10.1007/s10694-014-0411-8

[10]   Athenian, Ralph, et al. "On the Trajectories of Embers Initially Elevated or Lofted by Small Scale Ground Fire Plumes in High Winds." Fire Safety Journal, vol. 41, no. 5, 2006, pp. 349–363., doi:https://doi.org/10.1016/j.firesaf.2006.01.005.

[11]   Suzuki, Sakaya, et al. "Firebrands Generated from a Full-Scale Structure Burning under Well-Controlled Laboratory Conditions." Fire Safety Journal, vol. 63, 2014, pp. 43–51., doi:https://doi.org/10.1016/j.firesaf.2013.11.008.

[12]   Suzuki, S., Manzello, S.L. Experimental Study on Vulnerabilities of Japanese-Style Tile Roof Assemblies to Firebrand Exposures. Fire Technol 56, 2315–2330 (2020). https://doi.org/10.1007/s10694-020-00982-2

[13] Manzello, Samuel, and Sayaka Suzuki. "Influence of Board Spacing on Mitigating Wood Decking Assembly Ignition." *Fire Safety Journal*, vol. 110, Dec. 2019, doi:https://doi.org/10.1016/j.firesaf.2019.102913.

[14] Warey, Alok. "Influence of Thermal Contact on Heat Transfer from Glowing Firebrands." *Case Studies in Thermal Engineering*, vol. 12, Sept. 2018, pp. 301–311., doi:https://doi.org/10.1016/j.csite.2018.04.018.

[15] Hakes, Raquel, et al. "Thermal Characterization of Firebrand Piles." *Fire Safety Journal*, vol. 104, Mar. 2019, pp. 34–42., doi:https://doi.org/10.1016/j.firesaf.2018.10.002.

[16] Manzello, Samuel, et al. "Experimental Investigation of Firebrands: Generation and Ignition of Fuel Beds." *Fire Safety Journal*, vol. 43, no. 3, Apr. 2008, pp. 226–233., doi:https://doi.org/10.1016/j.firesaf.2006.06.010.

[17] Suzuki, S., Manzello, S.L. Investigating Coupled Effect of Radiative Heat Flux and Firebrand Showers on Ignition of Fuel Beds. Fire Technol (2020). https://doi.org/10.1007/s10694-020-01018-5

[18] Kim, Dennis, and Peter Sunderland. "Fire Ember Pyrometry Using a Color Camera." *Fire Safety Journal*, vol. 106, June 2019, pp. 88–93., doi:https://doi.org/10.1016/j.firesaf.2019.04.006.

[19] Urban, J.L., Vicariotto, M., Dunn-Rankin, D. et al. Temperature Measurement of Glowing Embers with Color Pyrometry. Fire Technol 55, 1013–1026 (2019). https://doi.org/10.1007/s10694-018-0810-3

[20] Urbas, Joe, et al. "Surface Temperature Measurements on Burning Materials Using an Infrared Pyrometer: Accounting for Emissivity and Reflection of External Radiation." *Fire and Materials*, vol. 28, no. 1, Jan. 2004, pp. 33–53., doi:10.1002/fam.844.

[21] Manzello, Samuel, et al. "Investigation on the Ability of Glowing Firebrands Deposited within Crevices to Ignite Common Building Materials." *Fire Safety Journal*, vol. 44, no. 6, Aug. 2009, pp. 894–900., doi:https://doi.org/10.1016/j.firesaf.2009.05.001.

[22] Sony RX10 III with F2.4-4 Large-Aperture 24-600mm Zoom Lens." *Sony*, Sony, www.sony.com/electronics/cyber-shot-compact-cameras/dsc-rx10m3/specifications.

[23] Sylramic SiC Fiber." *COI Ceramics*, ATK Space Systems, Jan. 2013, www.coiceramics.com/pdfs/Sylramic.pdf.

[24] Coffin, Dave. "DCRaw." *Softonic*, July 2020, dcraw.en.softonic.com/?ex=CORE-139.5.

[25] Araujo, Antonio. "Multi-Spectral Pyrometry—a Review." *Measurement Science and Technology*, vol. 28, no. 8, 17 July 2017.

[26] Tikkanen, Amy. "Lux." *Encyclopædia Britannica*, Encyclopædia Britannica, Inc., 2020, www.britannica.com/science/lux.

[27] Sunderland, Peter, et al. "Digital Camera Measurements of Soot Temperature and Soot Volume Fraction in Axisymmetric Flames." *Applied Optics*, vol. 52, no. 33, 2013, pp. 8040–8047., doi:https://doi.org/10.1364/AO.52.008040.

[28] Densmore, J. M. et al. "High-speed digital color imaging pyrometry." *Applied optics* 50 17 (2011): 2659-65 .

[29] "Recommended Lights Levels." NOAO, AURA, www.noao.edu/education/QLTkit/ACTIVITY_Documents/Safety/LightLevels_outdoor+indoor.pdf.

[30] Tohidi, Ali, and Nigel B. Kaye. "Stochastic Modeling of Firebrand Shower Scenario." Fire Safety Journal, vol. 91, July 2017, pp. 91–102., doi:https://doi.org/10.1016/j.firesaf.2017.04.039.

[31] Bergman, Theodore L., and Adrienne S. Lavine. Fundamentals of Heat and Mass Transfer. 8th ed., Wiley, 2017.

[32] Quintiere, James G. Fundamentals of Fire Phenomena. Wiley, 2008.

[33] Lu, Hong, et al. "Particle Surface Temperature Measurements with Multicolor Band Pyrometry." *AIChE Journal*, vol. 55, no. 1, Jan. 2009, pp. 243–255., doi:10.1002/aic.11677.

[34] Liu, Y., Urban, J.L., Xu, C. et al. Temperature and Motion Tracking of Metal Spark Sprays. *Fire Technol* **55,** 2143–2169 (2019). https://doi.org/10.1007/s10694-019-00847-3

[35] Wang, Z., Tam, W.C., Chen, J. *et al.* Thin Filament Pyrometry Field Measurements in a Medium-Scale Pool Fire. *Fire Technol* **56,** 837–861 (2020). https://doi.org/10.1007/s10694-019-00906-9

[36] Zander, Fabian. "Surface Temperature Measurements in Hypersonic Testing Using Digital Single-Lens Reflex Cameras." *Journal of Thermophysics and Heat Transfer*, vol. 30, no. 4, May 2016, pp. 1–7., doi:10.2514/1.T4820.

[37] Kuhn, Peter B., et al. "Soot and Thin-Filament Pyrometry Using a Color Digital Camera." *Proceedings of the Combustion Institute*, vol. 33, no. 1, 2011, pp. 743–750., doi:https://doi.org/10.1016/j.proci.2010.05.006.

[38] Xu, Yang, et al. "Measurement on the Surface Temperature of Dispersed Chars in a Flat-Flame Burner Using Modified RGB Pyrometry." *Energy & Fuels*, vol. 31, no. 3, Dec. 2016, doi:10.1021/acs.energyfuels.6b02203.

Appendix

RGB Pixel Value Extraction Code

```
A = imread('dsc04487.tiff');
d = 1815;
e = 2670;
c = linspace(e,e+161,162);
r1 = linspace(d,d,162);
r2 = linspace(d+1,d+1,162);
r3 = linspace(d+2,d+2,162);
r4 = linspace(d+3,d+3,162);
r5 = linspace(d+4,d+4,162);
r6 = linspace(d+5,d+5,162);
r7 = linspace(d+6,d+6,162);
r8 = linspace(d+7,d+7,162);
r9 = linspace(d+8,d+8,162);
r10 = linspace(d+9,d+9,162);
r11 = linspace(d+10,d+10,162);
r12 = linspace(d+11,d+11,162);
r13 = linspace(d+12,d+12,162);
r14 = linspace(d+13,d+13,162);
r15 = linspace(d+14,d+14,162);
r16 = linspace(d+15,d+15,162);
r17 = linspace(d+16,d+16,162);
r18 = linspace(d+17,d+17,162);
r19 = linspace(d+18,d+18,162);
r20 = linspace(d+19,d+19,162);
r21 = linspace(d+20,d+20,162);
r22 = linspace(d+21,d+21,162);
r23 = linspace(d+22,d+22,162);
r24 = linspace(d+23,d+23,162);
r25 = linspace(d+24,d+24,162);
r26 = linspace(d+25,d+25,162);
r27 = linspace(d+26,d+26,162);
r28 = linspace(d+27,d+27,162);
r29 = linspace(d+28,d+28,162);
r30 = linspace(d+29,d+29,162);
r31 = linspace(d+30,d+30,162);
r32 = linspace(d+31,d+31,162);
r33 = linspace(d+32,d+32,162);
```

```
r34 = linspace(d+33,d+33,162);
r35 = linspace(d+34,d+34,162);
r36 = linspace(d+35,d+35,162);
r37 = linspace(d+36,d+36,162);
r38 = linspace(d+37,d+37,162);
r39 = linspace(d+38,d+38,162);
r40 = linspace(d+39,d+39,162);
r41 = linspace(d+40,d+40,162);
r42 = linspace(d+41,d+41,162);
r43 = linspace(d+42,d+42,162);
r44 = linspace(d+43,d+43,162);
r45 = linspace(d+44,d+44,162);
r46 = linspace(d+45,d+45,162);
r47 = linspace(d+46,d+46,162);
r48 = linspace(d+47,d+47,162);
r49 = linspace(d+48,d+48,162);
row1 = impixel(A,c,r1);
row2 = impixel(A,c,r2);
row3 = impixel(A,c,r3);
row4 = impixel(A,c,r4);
row5 = impixel(A,c,r5);
row6 = impixel(A,c,r6);
row7 = impixel(A,c,r7);
row8 = impixel(A,c,r8);
row9 = impixel(A,c,r9);
row10 = impixel(A,c,r10);
row11 = impixel(A,c,r11);
row12 = impixel(A,c,r12);
row13 = impixel(A,c,r13);
row14 = impixel(A,c,r14);
row15 = impixel(A,c,r15);
row16 = impixel(A,c,r16);
row17 = impixel(A,c,r17);
row18 = impixel(A,c,r18);
row19 = impixel(A,c,r19);
row20 = impixel(A,c,r20);
row21 = impixel(A,c,r21);
row22 = impixel(A,c,r22);
row23 = impixel(A,c,r23);
row24 = impixel(A,c,r24);
```

```
row25 = impixel(A,c,r25);
row26 = impixel(A,c,r26);
row27 = impixel(A,c,r27);
row28 = impixel(A,c,r28);
row29 = impixel(A,c,r29);
row30 = impixel(A,c,r30);
row31 = impixel(A,c,r31);
row32 = impixel(A,c,r32);
row33 = impixel(A,c,r33);
row34 = impixel(A,c,r34);
row35 = impixel(A,c,r35);
row36 = impixel(A,c,r36);
row37 = impixel(A,c,r37);
row38 = impixel(A,c,r38);
row39 = impixel(A,c,r39);
row40 = impixel(A,c,r40);
row41 = impixel(A,c,r41);
row42 = impixel(A,c,r42);
row43 = impixel(A,c,r43);
row44 = impixel(A,c,r44);
row45 = impixel(A,c,r45);
row46 = impixel(A,c,r46);
row47 = impixel(A,c,r47);
row48 = impixel(A,c,r48);
row49 = impixel(A,c,r49);

Z(1:162,1) = 0;
B = [row1 Z row2 Z row3 Z row4 Z row5 Z row6 Z row7 Z row8 Z row9 Z row10 Z row11 Z
        row12 Z row13 Z row14 Z row15 Z row16 Z row17 Z row18 Z row19 Z row20 Z row21
        Z row22 Z row23 Z row24 Z row25 Z row26 Z row27 Z row28 Z row29 Z row30 Z row31
        Z row32 Z row33 Z row34 Z row35 Z row36 Z row37 Z row38 Z row39 Z row40 Z row41
        Z row42 Z row43 Z row44 Z row45 Z row46 Z row47 Z row48 Z row49];
```

Ember Analysis Code

```
A = imread('dsc04301.tiff');
rdc = 7.7;
gdc = 11.5;
bdc = 4.4;
iso = 100;
t = 0.004;
```

```matlab
f = 2.4;
r1 = 1810;
r2 = 1855;
c1 = 2690;
c2 = 2790;
nrows = r2-r1+1;
ncolumns = c2-c1+1;
B = zeros(nrows,3*ncolumns);
for i = 1:nrows
   for j = 1:ncolumns
      B(i,((3*j)-2):3*j) = impixel(A,c1-1+j,r1-1+i);
   end
end
rawred = B(1:end,1:3:end);
rawred2 = zeros(nrows,ncolumns);
for i = 1:nrows
   for j = 1:ncolumns
      if rawred(i,j) > 65534
         rawred2(i,j) = 0;
      else
         rawred2(i,j) = rawred(i,j);
      end
   end
end
rawgreen = B(1:end,2:3:end);
rawblue = B(1:end,3:3:end);
normred = ((rawred2-rdc)*(f^2))/(iso*t);
normgreen = ((rawgreen-gdc)*(f^2))/(iso*t);
normblue = ((rawblue-bdc)*(f^2))/(iso*t);
GR = normgreen./normred;
GR2 = log10(GR);
IP = imag(GR2);
logGR = zeros(nrows,ncolumns);
for i=1:nrows
   for j=1:ncolumns
      if IP(i,j) > 0
         logGR(i,j) = 0;
      else
         logGR(i,j) = GR2(i,j);
      end
```

```
    end
end
RT = (362.73.*(logGR.^3) + 2186.7.*(logGR.^2) + 4466.5.*(logGR) + 3753.5);
RT2 = zeros(nrows,ncolumns);
for i=1:nrows
   for j=1:ncolumns
     if RT(i,j) < 600
        RT2(i,j) = 0;
     elseif RT(i,j) > 1200
        RT2(i,j) = 0;
     else
        RT2(i,j) = RT(i,j);
     end
   end
end
RT3 = flip(RT2);
RT4 = zeros(nrows,ncolumns);
for i = 4:(nrows-4)
   for j = 4:(ncolumns-4)
     if nnz(RT3(i-3:i+3,j-3:j+3)) < 25
        RT4(i,j) = 0;
     else
        RT4(i,j) = RT3(i,j);
     end
   end
end
pcolor(RT4)
colormap jet
```

DCRAW input line

>dcraw -v -4 -T filename.arw

TECPLOT input line

>python -O ConvertExcelData.py largeinfile.xlsx outfile.dat